Modeling the Hydrodynamics, Sediment Transport, and Valley Incision of Outlet-forming Floods from Martian Crater Lakes

Caleb I. Fassett[1]
Timothy A. Goudge[2,3,4]

[1]NASA Marshall Space Flight Center, Huntsville, AL 35805
[2]Department of Geological Sciences, Jackson School of Geosciences, The University of Texas at Austin, Austin, TX, USA
[3]Center for Planetary Systems Habitability, The University of Texas at Austin, Austin, TX, USA
[4]CIFAR Azrieli Global Scholars Program, CIFAR, Toronto, Ontario, Canada

e-mail: caleb.i.fassett@nasa.gov
phone: 256-961-7446

Key Points:

1. Filling of crater lakes on Mars led to the formation of large outlet canyons due to basin-breaching flood events.
2. The physics and hydrodynamics of outlet-forming floods on Mars is described; transport of sediment in suspension was likely important.
3. Model runs for outlet-forming floods on idealized terrain and reconstructed Mars topography were completed, including for Jezero crater.

Abstract

Open-basin lakes that have outlets, formed where the stored water breached the basin-confining topography (e.g., crater rims), have been recognized on Mars for decades. However, the mechanics involved in formation of these outlets has not been studied in detail. Here, we study this outlet formation process through a series of numerical experiments accomplished by adding erosion and sediment transport routines to an existing hydrodynamic simulation, ANUGA. These experiments are consistent with outlets being carved in single flood events, at least if sediment was available throughout outlet formation as in a transport-limited regime. Peak discharges from these open-basin lakes, including from Jezero crater, were 10^4–10^6 m^3/s, and the outlet-forming floods lasted for days to weeks, depending on lake size. Moreover, we find that sediment transport by suspension was likely important during these floods – outlets could not have reached their observed sizes if flow was limited to bedload transport alone. This in turn may explain why small open-basin lakes are less commonly recognized on Mars, as small lakes had less inherent capacity to transport sediment in suspension and thus incise confining topography catastrophically. Geometry, topographic setting, and earlier fluvial valley development may have played a significant role in influencing the magnitude of outlet-forming floods and resulting outlet canyon incision.

Plain Language Summary

The landscape of Mars was once very different from today, as its ancient surface hosted hundreds of standing bodies of water. Some of these lakes filled enough to breach their confining topography forming an outlet valley, including Jezero crater where Perseverance is exploring today. Such a geologic interpretation is partially clear-cut, because the outlet valley would not exist if the lake had not filled with water. However, the associated outlet valley-forming events have not been examined in much detail in prior studies (with a few exceptions). These events are similar to floods from dam failures on Earth, as water in the lake perched above surrounding topography has substantial stored energy. Here, we develop routines to couple erosion and sediment transport to an existing hydrodynamic code and study the outlet formation process. We find that the size of lakes and their topographic setting on the martian landscape were important factors in controlling the erosion of their outlets. At least with our assumptions, we find that suspension of fairly sizable particles, at least the size of fine gravel, is necessary to match the outlet valleys that are observed, and that transport of grains along the bed alone was insufficient to match observations.

1. Introduction

That lakes once existed on the surface of Mars is no longer in serious dispute. Both in situ (e.g. Grotzinger et al., 2015) and orbital observations (e.g., Cabrol and Grin, 1998; Irwin et al., 2005; Fassett and Head, 2008; Goudge et al., 2015) strongly support the idea that Mars had standing water in its ancient past (e.g., Fig. 1a-c). Most lakes formed in impact craters, which were usually the local minima in martian topography, and crater rims commonly formed the

divide between drainage basins (e.g., Irwin et al., 2011). In instances where rivers or subsurface flow transported enough water into these basins to raise the lake level enough to breach these crater rims or divides (e.g., via overtopping, piping, or induced slumping), lake breach flood events occurred. In many instances, these outlets remain perched above the paleolakes' floors, allowing topographic recognition that they must once have been open-basin lakes (e.g., Fassett and Head, 2005, 2008; Fig. 1a-c).

On Earth, similar basin-breaching flood events occur both naturally and as the result of failures of constructed dams (e.g., O'Connor and Beebee, 2009). The geomorphological importance of natural lake-overflow events on Earth has seen renewed interest in the last decade (e.g., Lamb and Fonstad, 2010; Garcia-Castellanos and O'Connor, 2018; Hilgendorf et al., 2020). We recently compared the morphometry of the canyons that resulted from basin-breaching floods on Earth and Mars (Goudge et al., 2019). The observations in Goudge et al. (2019) suggest that events on both bodies share similar scaling properties based on the amount of erosion; past studies have also supported a common scaling based on comparisons of peak fluxes inferred from dam-breaks with channel dimensions (Irwin and Grant, 2009). On Mars, the large storage capacity of crater lakes led to numerous lake breach floods that carved significant outlet canyons (e.g., Irwin et al., 2002, 2004; Grant and Irwin, 2009) and the geomorphic work accomplished in the formation of these outlet valleys was globally significant (Goudge et al., 2021). With a few exceptions (e.g., Irwin et al., 2004; Coleman, 2013, 2015; Marra et al., 2014; Warren et al., 2021), however, the morphodynamics, hydrodynamics, and controls on basin-breaching flood events on Mars remains to be investigated. These topics are the focus of the numerical modeling we pursue in this paper.

The basic scenario that leads to basin-breaching flood events is shown in Figure 1d. A large amount of water can be stored in a crater lake, impounded by the crater's rim or wall and other surrounding topography elevated above the lake floor. This stored water has a great deal of potential energy. When the lake impounding topography is overtopped or fails due to a mechanism like piping or collapse, water begins to spill out of the lake. If the water initially discharged is sufficient to erode the dam, or the dam is otherwise failing, a breach will grow, and a positive feedback is set up between discharge and incision of the breach (Garcia-Castellanos and O'Connor, 2018). The water spilling through the breach has significant capacity for geomorphic work and can then incise and carve an outlet canyon connected to the breach. An interesting element of some martian crater lakes is that the lake floors of the basins extended substantially below regional topography (e.g., Fassett and Head, 2008), so the outlet breach does not have to erode just a narrow dam to progressively release its stored water and energy, but instead incises into a more extensive regional confining volume. Ultimately, as the lake drains, the outlet's discharge of water Q peaks and then declines in concert with its capacity to erode the confining topography (O'Connor and Beebee, 2009; Garcia-Castellanos and O'Connor, 2018). It is possible that incision of the outlet can occur over long periods of time if the lake continues to

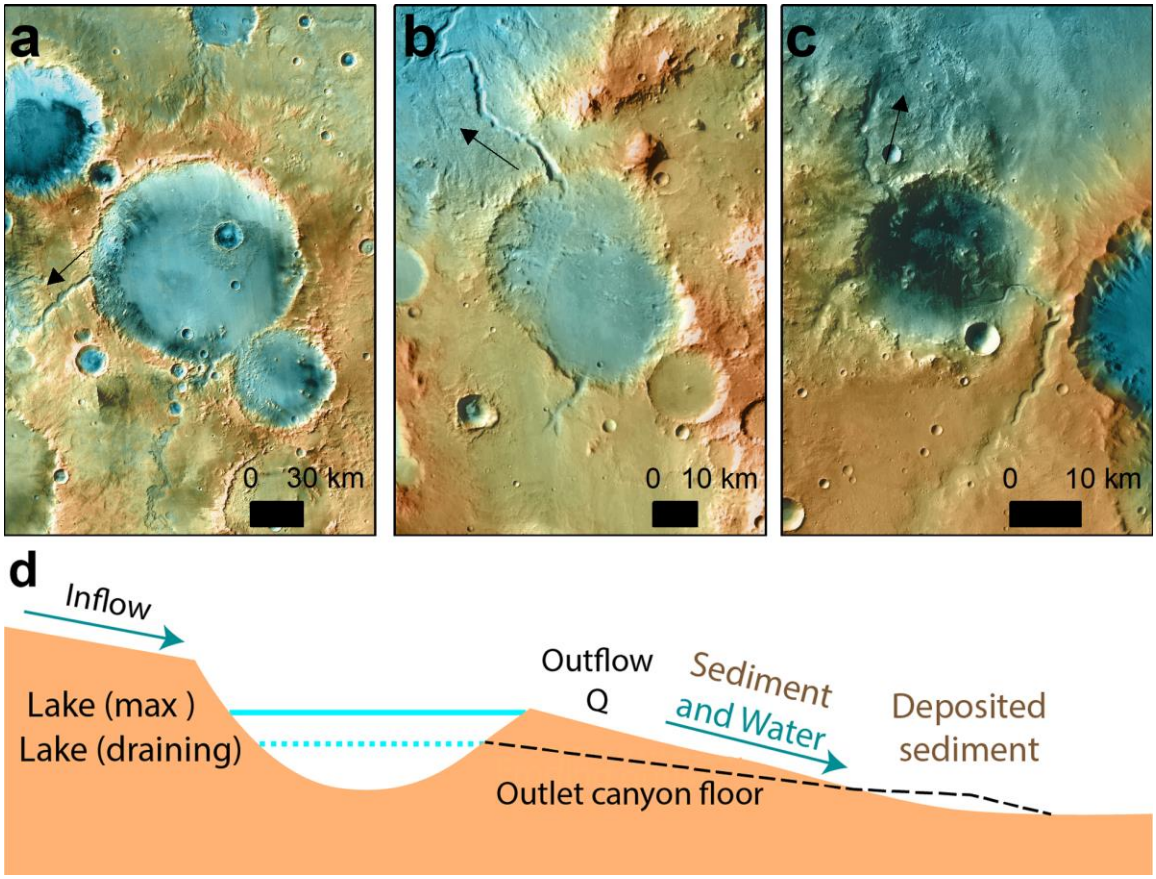

Fig. 1. Open-basin lakes are interpreted to have outlets (black arrows showing flow direction) formed by rim-breach flood events. (a) Mädler crater (Howard, 2007), Lake 19 in Fassett and Head (2008); (b) an unnamed crater in Libya Montes (Cabrol and Grin, 2001), Lake 25 in Fassett and Head (2008) (c) Milna crater (Buhler et al., 2014), Lake 65 in Fassett and Head (2008). (d) Cartoon of lake breach flooding. After a lake forms, lake level will rise if sufficient inflow (in excess of evaporation, plus net groundwater) occurs to add water to the lake (e.g., Stucky de Quay, 2020). How the lake fills up via this process is important to establish the conditions for flooding (storing water), but irrelevant to the dynamics of the outflow event, which is controlled by the erosion of the outlet. As illustrated in this study, numerous factors influence outlet erosion, particularly the size of the lake, regional topography, and the erodibility of the substrate. Examples (a-c) are shown with topography from MOLA&HRSC blend (Fergason et al., 2018) and CTX mosaic (Dickson et al., 2018)

see input sufficient to allow it to overspill. However, ongoing incision of large martian paleolake outlets appears to have been of limited importance given that the scaling of lake outlet geometry is strongly controlled by the amount of water that could be stored in the lakes prior to breaching (Goudge et al., 2019). Some smaller lake outlets formed during the Hesperian and Amazonian may record multiple flooding cycles (Warren et al., 2021), but this does not appear to be the norm for larger lakes formed earlier in Mars history, where a single catastrophic flood appears sufficient to explain observations (see also results and discussion).

The relative simplicity of this description belies a series of challenges for reconstructing and modeling outlet-forming floods. The first such challenge is that the evolving flood

hydrograph is directly coupled to the erosion and transport of sediment (Garcia-Castellanos and O'Connor, 2018). Well established and sophisticated models exist that are capable of routing floods upon existing topography, but because of the feedback between discharge and breach growth, fully modeling both topographic adjustment and sediment transport (i.e., morphodynamics) is critical to capture the formation of an outlet canyon (e.g., Baynes et al., 2015). Additionally, the accurate parameterization of sediment transport for these events is a perilous proposition, especially given the large flood stages and transport under Mars gravity (e.g., see discussion in Kleinhans, 2005). These events were well outside the range of normal terrestrial conditions where semi-empirical sediment transport relations have been defined, calibrated, and verified.

The second challenge, common to almost all studies seeking to reconstruct hydrology and sediment transport on Mars, is that major uncertainty exists in the nature of the material eroded and transported. For example, we would expect that an outlet carved into a weakly lithified sandstone would erode much more efficiently than an outlet breach carved into basaltic bedrock. Yet from remotely sensed observations, it can be hard or impossible to establish definitively basic properties relevant to incision, like effective grain size, material strength, cohesion, and bed roughness, especially beneath the uppermost surface. The potential parameter space is thus rather large. We simplify this problem by assuming that sediment was available for transport given sufficient shear-stress, and that erosion is transport-, not detachment-, limited. We argue that this is consistent with a paradigm that the martian highlands crust is dominated by relatively weak and friable materials (e.g., Rogers et al., 2018), as well as the hypothesis that catastrophic lake breach floods on Earth maybe treated as transport-limited (e.g., Lamb and Fonstad, 2010). This simplification does limit the applicability of our study if outlets were carved into massive bedrock that needed to be weathered to become transportable, or if the effective grain size of sediment being transported was >8-10cm.

A third challenge for reconstructing the behavior at a particular location is that modeling the outlet formation after the fact requires reconstructing topography prior to the event, which has to be inferred from modern topography and thus has inherent limitations (e.g., Barnhart et al., 2009). Finally, a fourth challenge is that there is no obvious predefined criterion for what constitutes a high-fidelity reconstruction of one of these flood events by a model. The outlet canyon carved in the numerical models will never perfectly match the topography observed today on Mars, so evaluating the best reconstruction of the event requires consideration of appropriate qualitative and quantitative metrics (e.g., Barnhart et al., 2009).

We have worked on this problem and made some progress towards each of these challenges, as we discuss in detail in this paper. We have developed procedures that couple sediment transport to fluid flow in the open-source hydrodynamic modeling package, ANUGA (e.g., Roberts et al., 2019; Rigby and Van Drie, 2008; https://anuga.anu.edu.au/; https://github.com/GeoscienceAustralia/anuga_core). We then used this model to run test examples in two types of domains: (1) idealized crater lakes, and (2) a few reconstructed Mars

lakes, including Jezero crater. The grain size of the material transported in the flood was varied over a significant range to address the uncertainty in that parameter (though it was fixed across the domain for a given model). We also experiment with different sediment transport mechanisms and other physical parameters. We use these results to develop an understanding of the hydrodynamics and sediment transport involved in lake outlet-forming floods on Mars.

2. Modeling Methods

2.1. Introduction to ANUGA

ANUGA is an open-source finite volume model that solves the shallow water equations (depth-integrated Navier-Stokes) (Roberts et al., 2019; Rigby and Van Drie, 2008). The code is written in python with C extensions, and the code relies upon numpy routines and data structures (van der Walt et al., 2011). The ANUGA model domain is discretized as a triangular mesh that the user can define. Both the topography and the initial water stage in the domain can be either defined on this mesh or imported from data.

The default ANUGA code base does not include any alteration of topography with time, but instead focuses on the routing of fluid flow. However, it is possible to define custom operators that do alter topography and thus enable erosion and deposition on the domain. Some erosion operators developed for ANUGA are distributed with the code. One such operator calculates erosion due to shear on the bed, but is not focused on morphodynamics and sediment transport, so does not conserve sediment (e.g., Van Drie et al., 2013). Another ANUGA operator looks at the erosion of dunes (Rigby et al., 2017). Finally, a separately distributed sediment transport operator focused on suspended sediment was developed called AnugaSED (Perignon, 2016). Our own work is both inspired by and descended in part from all these earlier open-source examples, particularly Perignon (2016), as described below.

To address the problem of lake outlet evolution from lake breach flooding, we defined four custom operators to implement sediment transport: (1) a bedload transport operator; (2) a sediment suspension and advection operator; (3) an operator that allows dynamic redefinition of bed friction, and (4) an operator that reduces steep slopes to a specified angle of repose. We discuss details of these operators' physics implementation and known limitations in turn below.

2.2. ANUGA operators and sediment transport physics

2.2.1 Bedload transport operator

To add sediment erosion and bedload transport to ANUGA, we follow a standard approach that relates sediment transport capacity to excess shear stress (e.g., Parker, 2005; see also Kleinhans, 2005). This type of approach has been used before when reconstructing sediment transport associated with dam breach events (e.g., Lamb and Fonstad, 2010). Specifically, we calculate the shear stress along the bed, τ, as:

$$\tau = \rho f_c v^2 \qquad \text{eq. 1}$$

where the friction factor f_c here is the Darcy-Weisbach friction factor divided by 8, v is the magnitude of the flow velocity observed in the cell, and ρ is the water density. This non-dimensionalizes to τ^*:

$$\tau^* = \frac{\tau}{(\rho_s - \rho)gD} \qquad \text{eq. 2}$$

where ρ_s is the grain density, g is the gravitational acceleration, and D is the grain size. Then, the excess shear x is calculated above a critical shear stress required to initiate sediment transport, τ_c^*:

$$x = \tau^* - \tau_c^* \qquad \text{eq. 3}$$

How this excess shear stress on the bed translates into a functional description of sediment transport has been subject to a great body of literature, reviewed in the context of sediment transport on Mars by Kleinhaans et al. (2005). A common characteristic of many such functions is that they are expressed as a power law where nondimensional sediment flux q_b^* is a nonlinear function of excess shear:

$$q_b^* = Kx^m \qquad \text{eq. 4}$$

K is an empirical constant, and m is the power-law index.

We have applied two basic parameter sets to equation 4: (1) a classic stream-power bedload-only transport model, in the tradition of Meyer-Peter and Mueller (1948), but with a lower K based on the reanalysis of Wong and Parker (2006) (e.g., their eq. 24), and (2) the Engelund and Hansen (1967) transport model, which was based on combined suspension and bedload sediment flux. Note the difference in the exponent m that controls the non-linear dependence of sediment transport on excess shear stress differ in these two cases. It has also been suggested that larger m values of 3 or above may be relevant to extremely large flood events where cavitation may be important (Whipple et al., 2000). However, the importance of that mechanism for sediment transport in scenarios like those we study here remains poorly understood.

	Wong-Parker (2006)	Engelund-Hansen (1967)
K	4.0	$0.8/f_c$
$\tau_c{}^*$	0.04	0
m	1.5	2.5

Table 1. Parameterization for bedload based on Wong and Parker (2006) and combined bedload and suspended sediment transport after Engelund and Hansen (1967).

The nondimensional sediment flux from equation 4 can be converted to a dimensional sediment flux per unit width q_b (units $(m^3/s)/m$) as:

$$q_b = q_b^* \left\{ g(\frac{\rho_s}{\rho} - 1) \right\}^{0.5} D^{1.5} \qquad \text{eq. 5}$$

From equation 5, determining the erosion in each cell of the mesh requires the Exner equation:

$$\frac{dz}{dt} = -\left(\frac{1}{(1-\varphi)}\right)(\nabla \cdot q_b) \qquad \text{eq. 6}$$

φ here is porosity, which we take in most model runs in this paper as 0.2 (see also Suppl. Text S5). Solving equation 6 requires having q_b(equation 5) partitioned into appropriate vectorial components. To do so, we follow the suggestion that the sediment transport vector should parallel the vector for boundary shear stress (eq. 2.11 and 2.12 in Parker (1998)).

Implementation of these equations in our ANUGA bedload operator is nearly literal, but there are a few caveats. First, an issue caused by the discretization of the mesh leads to imperfect handling of erosion and deposition. In many model runs, this creates small (~1%) sediment volume/mass conservation errors that we have been unable to correct. Conceptually this is equivalent to a sediment volume lost by advection out of the domain without intermediate deposition. Second, we invoke an arbitrary maximum incision rate (*maxdz*) to maintain numerical stability. If any cell in the domain is above this max rate, we forcibly rescaled the amount of erosion in all changing cells by this maximum rate. The *maxdz* used in our modeling is nonphysically large (Table 2) and seldom comes into effect; when it occurs, it acts as an artificial reduction in the sediment transport efficiency through the domain.

2.2.2 Suspended Sediment Operator

For model runs that used the bedload operator (e.g., Meyer-Peter and Mueller (1948) and Wong and Parker (2006)), we added an additional sediment transport operator (not applied when using Engelund and Hansen (1967) because that already implicitly incorporates suspended sediment transport). Conceptually, the new suspended sediment operator uses excess shear stress to entrain sediment, rather than move it along the bed. Additionally, sediment settles out of the column, which has an average sediment concentration that advects with the flow. The net balance of sediment entrained and sediment that settles controls whether or not the suspended sediment component of *dz* is positive or negative for a given cell at a given timestep.

Following Smith and McLean (1977) and Parker (1998), in cells that have excess shear stress, the dimensionless entrainment rate E^* at a given timestep is given as:

$$E^* = 0.65 \left(\frac{\gamma_0 \left(\frac{\tau^*}{\tau_c{}^*} - 1 \right)}{1 + \gamma_0 \left(\frac{\tau^*}{\tau_c{}^*} - 1 \right)} \right) \qquad \text{eq. 7}$$

where τ^* is defined in eq. 2, τ_c^* is a critical shear stress for suspension (we use 0.04), and γ_0 is an empirical constant, $\gamma_0 = 0.0024$. A settling velocity v_s is calculated using Dietrich (1982)'s equation 5-9 (see supporting text S1). Combined with eq. 7 above, the results are a dimensional entrainment rate $E=v_sE^*$.

Determining the flux of sediment to the bed requires estimating the concentration of sediment in the bottom of the water column, c_b. Inspired by the approach of Davy and Lague (2009) and Ganti et al. (2014), we compute a suspended sediment distribution parameter d^*, which describes the relative proportion of sediment concentrated in the bottom layer compared to the average sediment concentration, $\bar{c}$. d^* is taken as a function of the Rouse number, $Z = v_s/\kappa u_s$, where v_s is the settling velocity from Dietrich (see supporting text S1), κ=0.41 (von Karman's constant), and $u_s = \sqrt{\tau/\rho}$. Then, the concentration in the bottom layer goes as $c_b = \bar{c}d^*$. Figure 2 shows how we assign d^* to vary with the Rouse number (supporting text S2). Finally, the deposition rate is $D=c_b v_s$, and

$$\frac{dz}{dt} = \left(\frac{1}{(1-\varphi)}\right)(D-E) \qquad \text{eq. 8}$$

The average sediment concentration $\bar{c}$ is tracked in each triangle, so that after each timestep the concentration is recalculated from the existing sediment volume, modified with the net entrained (or settled) volume from the bed. Sediment is only added to the water column up to an arbitrary maximum concentration, which we took in all runs as 30% by volume. This is important in the experiments with the smallest grain sizes (1-2mm). Likewise, for net deposition, the maximum thickness of deposited sediment is limited by the total volume of suspended sediment for that cell. In addition, *dz/dt* is limited to a *maxdz* here as well (as for bedload transport). Once erosion and deposition has occurred, sediment concentrations are altered in the domain by advecting suspended sediment along with the fluid. The implementation of that element of the operator is highly indebted to work previously by Perignon (2016).

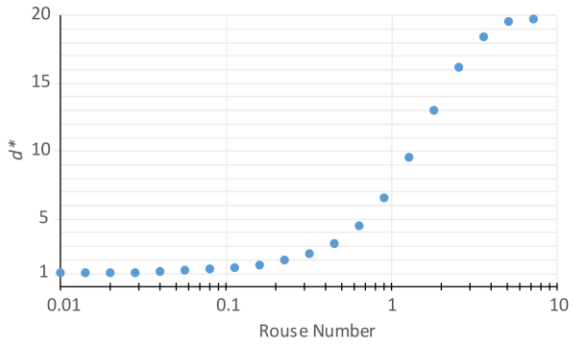

Figure 2. d^* as a function of Rouse number in the suspended sediment operator. For small Rouse numbers, sediment is evenly dispersed in the sediment column and substantial suspended sediment moves as washload. At high Rouse number, most sediment is near the bed (see, e.g., Ganti et al., 2014; supporting text S2).

Like the bedload operator, there are a few known limitations in the implementation of this operator. First, there is an obvious limitation imposed by the somewhat arbitrary nature of the concentration profile as a function of Rouse number (Fig. 2; supplemental text S2). Second, the suspended sediment does not modify the properties of the flow (i.e., the fluid density does not change, and the effect of

suspended sediment on the fluid's momentum is ignored). The second of these assumptions is reasonable for typical fluvial behavior but may be problematic for the kind of highly energetic events studied here, which could easily have debris flow-like behaviors, at least during early flood stages (e.g., Goudge et al., 2019). Unlike the bedload transport operator, this operator conserves sediment volume without issue.

2.2.3 Friction Operator

In ANUGA, the resistance to water moving over the mesh is specified with a Manning friction, *n*. The specified bed friction (Darcy-Weisbach *f*) also influences the sediment transport operators described above (note that in equation 1, $f_c = f/8$). Via the Darcy-Weisbach and Manning equations (see Wilson et al., 2004; eqs. 3 and 4), these are related by equation 9, where *h* is the depth of flow:

$$\sqrt{\frac{8}{f}} = n^{-1} g^{-0.5} h^{1/6} \qquad \text{eq. 9}$$

We implement a custom friction operator in ANUGA that allows a choice of one of three different parameterizations of friction. First, we define a mode based on Wilson et al. (2004)'s equations 13-15, where the Darcy-Weisbach *f* is specified as an empirical function of grain-size and flow depth *h* (see supporting text S3 for details). The Manning *n* is then spatially variable and calculated using eq. 9 at every time step.

Second, we provide a mode that follows Larsen and Lamb (2016) (see also Johnson, 2014), and calculate a constant *n* from equations (3) and (4) of their methods with specified bed roughness characteristics and parameters (k_s, r_d, and b_r). As a third option, we allow the user to simply specify Manning's *n* as a constant. With either the Larsen and Lamb (2016) option or when specifying *n* directly, we assume *n* does not vary spatially or temporally. Regardless, however, for all friction parameterizations, the friction factor for the purpose of sediment transport varies at each mesh cell at each timestep because it is a function of the evolving flow depth *h* (see eq. 9, and for the Wilson et al. (2004) method, supporting text S3).

2.2.4 Angle of Repose Operator

Avoiding element-to-element slopes in the mesh that exceed physically reasonable values required an operator to limit slope. To do so, we created an angle of repose operator that limits slopes in the model domain to a specified value. Wherever this slope angle is exceeded, bed topography is near-instantaneously diffused until it falls below the threshold. This method is not meant to reflect the underlying physics of bed slope failures, which are advective, but to act as a simple heuristic to avoid breaking other elements of the model that fail when slopes become too steep. The use of this operator for numerical stability also limits the steepness of canyon walls and knickpoints. Knickpoint retreat is physically plausible in outlet forming-floods (e.g., Lapôtre

and Lamb, 2015; Lapôtre et al., 2016), and observed in the outlets of some Mars open-basin lakes (e.g., Goudge and Fassett, 2018), so this limitation may be worth addressing in future work.

2.3 Metrics for Analyzing Results

There is not a single set of well-defined metrics that fully capture the outcome of the numerical experiments, or their behavior with time, but we found it necessary to define four parameters that we consistently used to analyze our results: breach depth, breach cross-sectional area, eroded volume, and discharge through the outlet as a function of model time.

The first two of these parameters characterize the breach morphometry and were both calculated at a fixed location based on the position of the initial breach (Fig. 3). Breach depth was defined as the maximum observed erosion in meters, computed by differencing the final and initial topography in the model sampled along a polyline defined by the initial breach location. Likewise, the cross-sectional area in square-meters was determined using rectangular integration (Riemann summing) of the difference between the final and initial outlet topography across the breach. In practice, breach depth and cross-sectional area were highly correlated, as might be expected.

Eroded volume (in m^3) was computed only in the outlet part of the domain downstream from the initial breach (Fig. 3) by summing up the change in topography of triangles only where erosion occurred (where final minus initial topography was negative), and multiplying by triangle area. Note that eroded volume metric is affected, albeit indirectly, by the sediment deposition in the domain resulting from the reflective boundary condition (see Section 3). As a lake at the end of the outlet forms and rises, an aggrading delta forms, which leads to a transition from erosion to deposition that slowly shifts back towards the lake. The eroded volumes we determined are influenced, but not dominated, by this behavior.

The last metric we broadly consider is the discharge (flux, hydrograph) of the floods, which are determined across the domain at the initial breach location . This is determined at each time-step using the built-in ANUGA method to *get_flow_through_cross_section* and reported n m^3/s.

Parameter	*Symbol*	Value, function, *or Range* [when range, default choice in brackets]	*Relevant Experiments* / Discussion
Varied Parameters			
Lake Radius	R	*1–20 km, a few experiments larger* [12 km]	*3.1.1*
Regional Slope	s	*0.5%-11%* [1.5%]	*3.1.2*
Confining Cross-Slope	s_2	*0.25%-8%* [1.5%]	*3.1.3*
Grain size	D	*1 mm – 8 cm* [8mm, 1 cm]	*3.1.1, 3.2.1*
Sediment Transport Law		*Bedload/Wong-Parker* *Engelund-Hansen* *Suspension-only* *[Bedload + Suspension]*	*3.2.1*
Friction Parameterization		Wilson et al. (2004) (variable n) for a given grain size and flow depth Larsen and Lamb (2016) [Constant n: 0.0545]	*3.2.2*
Gravity	g	[3.7], 9.8 m/s^2	*3.2.2*
Physical Constants			
Water density	ρ	1000 kg/m^3	*Suppl. Text. S4*
Sediment density	ρ_s	*2700-3300 kg/m^3* [3000 kg/m^3]	*Suppl. Text. S4*
Porosity	φ	[20%], 40%	*Suppl. Text. S5*
Artificial Constants			
Maximum dz/dt		5 m/s	2.2.1, 2.2.2
Angle of Repose		35˚	2.2.4

Table 2. Model parameters, variables, and constants for the idealized experiments in section 3.

3. Results: Idealized Model Runs and Parameter Sensitivity

In this section, we describe a series of experiments in an idealized domain (Figs. 3, 4) to understand the effect of various physical parameters (Table 2). The variable space for this problem is very large, and the nonlinear relationships between parameters can lead to complicated feedbacks that are hard to anticipate. Given the large parameter space and idealized nature of the domain, we have no expectation that this type of model will reproduce flood conditions like those on Mars with any exactitude. Instead we aimed to broadly explore the conditions controlling lake-breach floods, with the aim of understanding the model physics, generating multiple hypotheses, and providing an order-of-magnitude comparison against observational results.

For these idealized experiments, we divided the domain into three parts: the lake, the outlet zone, and a flat extended zone with no topography (Fig. 3). A range of boundary conditions are possible in ANUGA, but for numerical stability reasons, all model runs in this study used a reflective boundary on each edge. This led to standing bodies of water and deposition at the end of the evolving outlet. The extended zone in the domain, where this lake forms, is intended to help limit the influence on the results we discuss here. The topography of the crater holding the lake was assigned the shape of an ellipsoid with a maximum depth of $h_{lake}=25.7R^{0.62}$ for lake radius R. This was chosen to approximately match how the volumes of open basin lakes on Mars scaled as inferred by Fassett and Head (2008). The outlet zone had a

specified surface slope and cross-slope (see Fig. 3 and sections 3.1.2-3.1.3). Water and sediment was transported downstream beyond the outlet zone into the flat extended zone as the experiments progressed.

In typical experiments, the lake and extended zone were defined with a mesh resolution (typical triangle length scale) of 0.1*R*, equivalent to triangles with average linear dimension of ~1 km for a 10 km radius lake. A much finer, higher resolution mesh was defined in the outlet zone, as well as slightly inside the interior of lake to slightly into the flat extended zone (see Fig. 3), where all the prominent topographic changes occurred. In that area, the mesh resolution was typically set to 0.005*R* (50 m for a 10 km radius lake). The actual size of triangles varies slightly due to the mesh generation algorithm used by ANUGA (Shewchuk, 1996). For these idealized models, the flood was initiated by starting with a triangular notch three mesh elements wide at the breach location, with an initial 1:10 depth:width aspect ratio. Preliminary runs indicated that the precise dimensions of this initial notch had minimal effect on the resultant flood characteristics.

We show an illustration of results from one of the idealized runs with radius of 12 km in Figure 4. This is a typical case for the idealized modeling; the flux increased as the breach grew, then declined as the draining lake lost capacity to erode the breach. The outlet canyon for this example was mostly carved in a period of a few days near the peak of the flood. As is seen ubiquitously in these numerical experiments, some erosion took place inside the draining lake, which speaks to the power of these catastrophic events. This is also observed in many Mars open-basin lakes.

Preliminary results led us to hypothesize that the geometry of the lake and its surroundings play a significant – possibly pre-dominant – role in the magnitude of the flood and the erosion that occurs following the breach event. We first test this idea by exploring variations in lake size and grain size (3.1.1), exterior slope (3.1.2), and confining slope (3.1.3). Then, we experiment with the defined sediment transport physics (3.2.1) and compare Earth and Mars gravity (3.2.2).

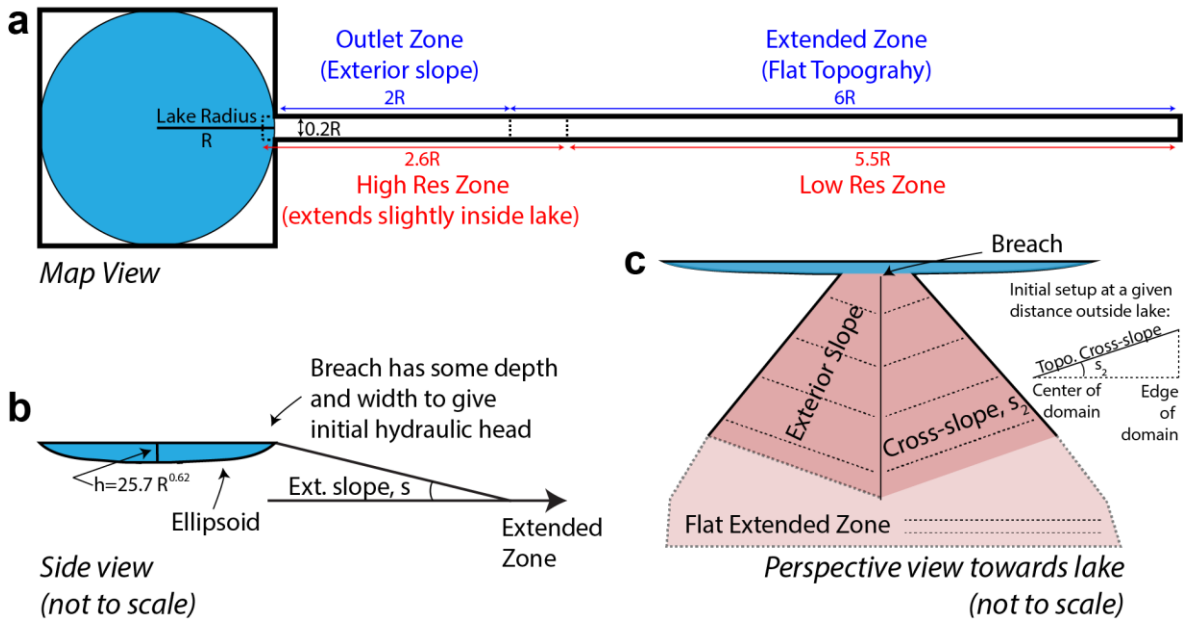

Figure 3. Illustration of the idealized model setup for section 3. Note the lake depth in these experiments was chosen so that lake volume would scale with lake radius / area consistent with Fassett and Head (2008), $V \sim R^{2.6}$.

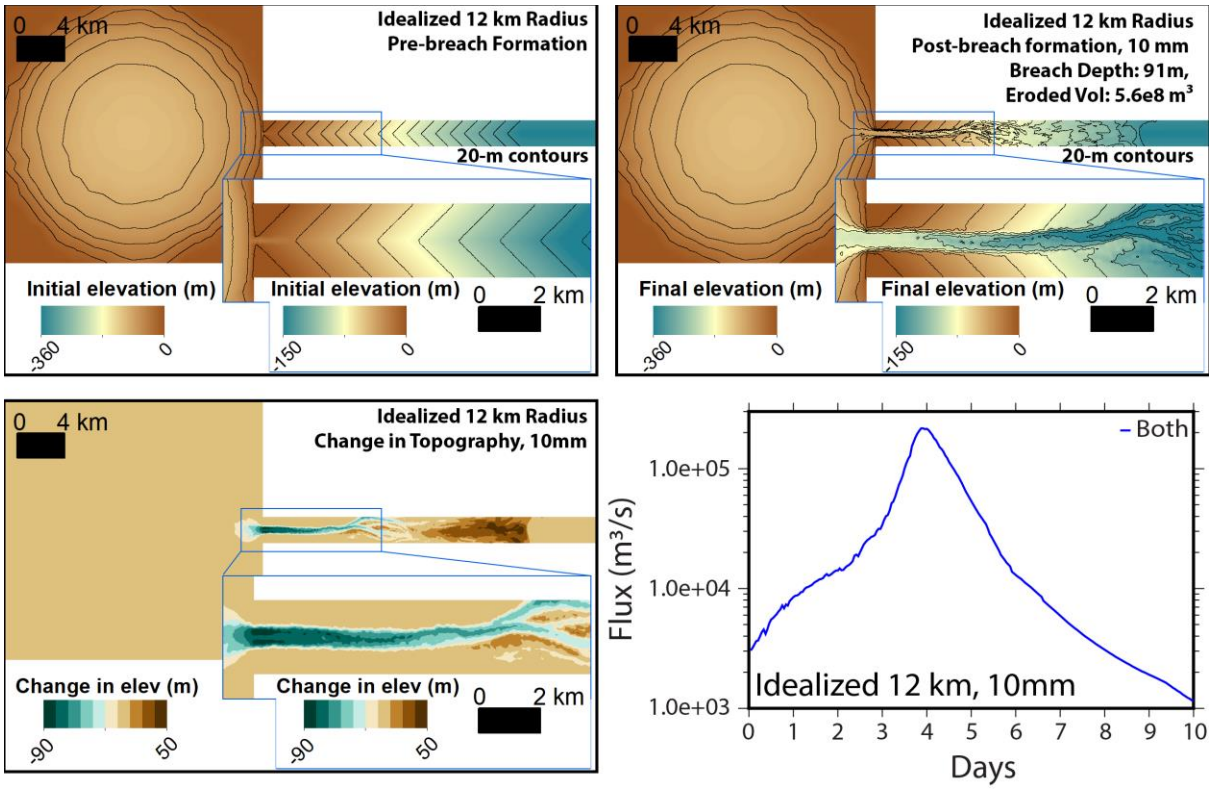

Figure 4. An example of an idealized model run for a 12 km radius crater. Grain size in the domain was set to 10 mm. Other parameters were set at the defaults given in Table 2. The initial stage was set above a narrow initial notch in the crater rim. As the flood grew, a larger breach grew, rapidly draining the lake.

3.1 Lake Geometry, Topography, and Erosion

3.1.1. *Variations in Lake Size and Grain Size*

Open basin paleolakes on Mars vary in area from ~10^0– 10^5 km^2, equivalent to being circular craters of ~0.6– 400 km in radii. There is an increase in the number of observed paleolakes on Mars as size decreases (Fassett and Head, 2008; Seekell and Pace, 2011), although at areas <~100 km^2 (radius of ~5.6 km) paleolakes become less common, most often interpreted as an observation/preservation bias (e.g., Cabrol and Grin, 2010). *Goudge et al.* (2019)'s results suggested that drained volume, which is ultimately controlled by lake size, was the primary control on the amount of erosion outlets experienced in basin-breaching floods, consistent with the intuition that the stored energy in the lake is the most important factor for this problem. The maximum lake size we explored in this particular experiment had radius of 20 km, roughly equivalent to the size of Jezero crater (Fassett and Head, 2005, 2008). This upper limit was chosen as a practical convenience given that computational times rapidly increase with the total number of mesh cells, and we wished to maintain a reasonable mesh resolution in the domain.

Figure 5 shows the dependence of breach depth, breach cross-sectional area, and total eroded volume on lake size. As expected, lake size is a major control on the magnitude of modeled erosion for parameters related to the breach as well as the total eroded outlet volume.

Secondarily, in these experiments, the grain size induced additional variation in total erosion in a given flooding event, with larger grain size resulting in reduced erosion, as expected. At the 8 mm and 1 cm grain sizes, lakes smaller than 8 km failed to have runaway flood events, at least with the initial conditions, model setup, and physics assumed here. We again explicitly note that the grain size used here is not meant to be exactly representative of what would have existed on Mars, which undoubtedly had a range of grain sizes, but to parameterize sediment transport in the model. There are also many other terms that affect the model's resistance to sediment transport that we do not usually vary, including crustal porosity and the leading coefficients on the applied sediment transport laws.

3.1.2. *Varying Exterior Slope*

Figure 6 illustrates how erosion varied as a function of slope at a fixed lake size (12 km radius) and grain size (8mm). The exterior slope is an important control on erosion of the outlet in two respects. First, steeper exterior slopes reduce the volume of the wedge of sediment (i.e., the impoundment volume) that needs to be removed as a lake basin is draining (e.g., Fig. 1, 3b). Second, higher slopes enhance the velocity and hence bed shear stress of the flood. Most open-basin lakes on Mars have exterior slopes between 0.5 and 2%, though a few are steeper and a few are shallower, in line with the broader inter-crater slopes in the southern highlands (e.g., Irwin et al., 2011).

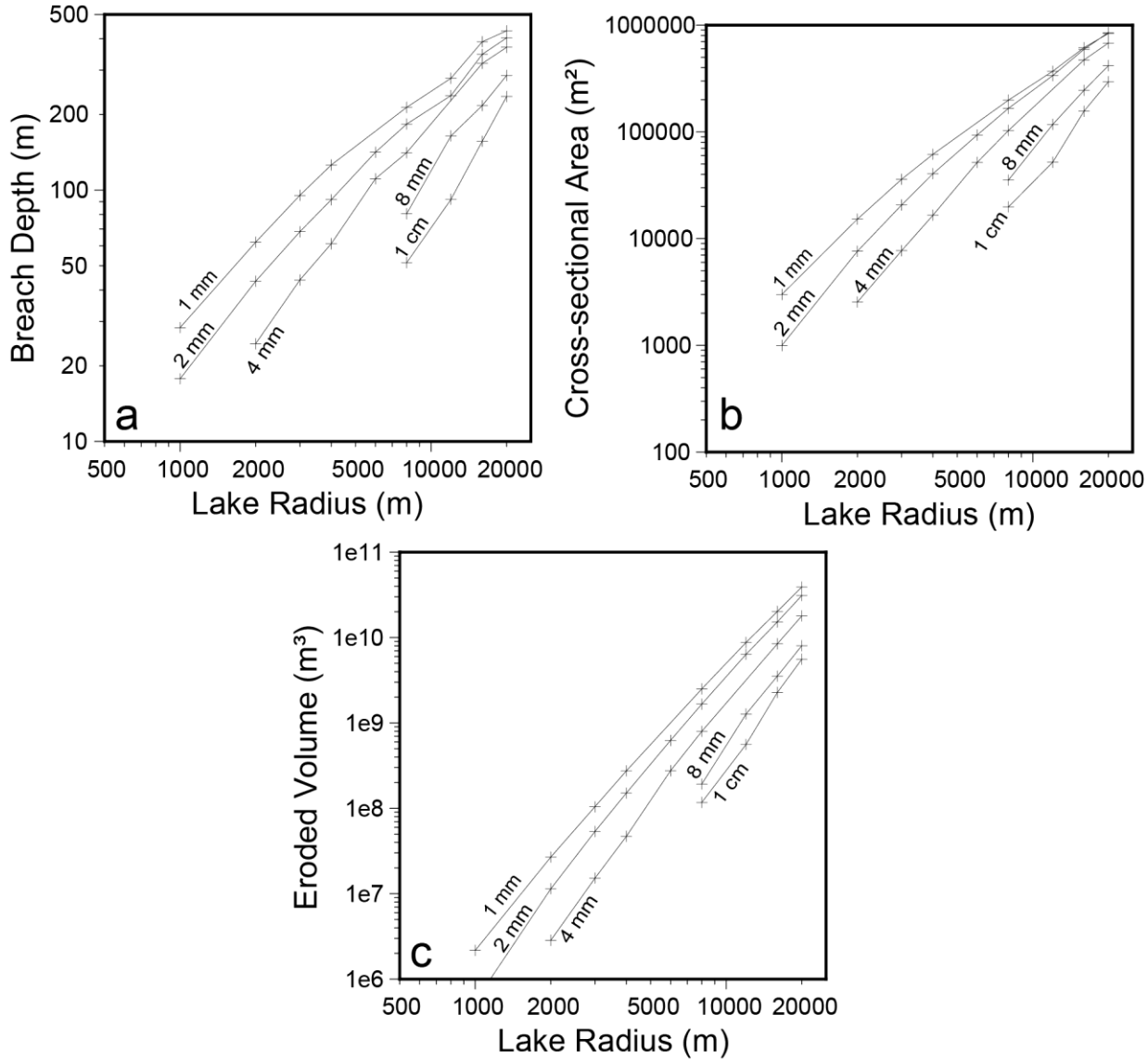

Figure 5. (a) Breach depth, (b) breach cross-sectional area, and (c) total eroded volumes as a function of lake radius and grain size in the idealized model runs. Except for grain size and lake radius, all other parameters were set to the defaults in Table 2.

There are a few main takeaways from this set of experiments, keeping in mind that the specifics would vary with different grain size or lake size. The overarching observation is that slope is an important factor in controlling outlet erosion. Under the chosen conditions, the initial lake completely drained above ~3% slope, and almost completely drained at 2% slope (98% of the lake's initial volume). Interestingly, the amount of erosion in the outlet varied as a function of the exterior slope, even in these completely drained instances. For these floods, which had essentially the same total amount of water discharge, the increase in total eroded sediment was linear with *s*, suggesting that the additional incision was proportional to the additional bed shear stress available at higher slopes.

Below slopes of 1%, lake drainage in this experiment was incomplete. In this regime, the total amount of erosion that occurs is dependent both on the amount of water released from the lake (more at steeper slopes, since a deeper outlet was cut) and the amount of geomorphic work this water could do (also more at steeper slopes, as above). The combination of these two effects makes the eroded volume a much stronger function of slope below 1% slope than above it (Fig. 6). Thus, the amount of incision drops rapidly from >100 m at 1.4% to ~10m at 0.5%. A way to think about this is that breaching a deep crater lake onto low-sloped surroundings is equivalent to

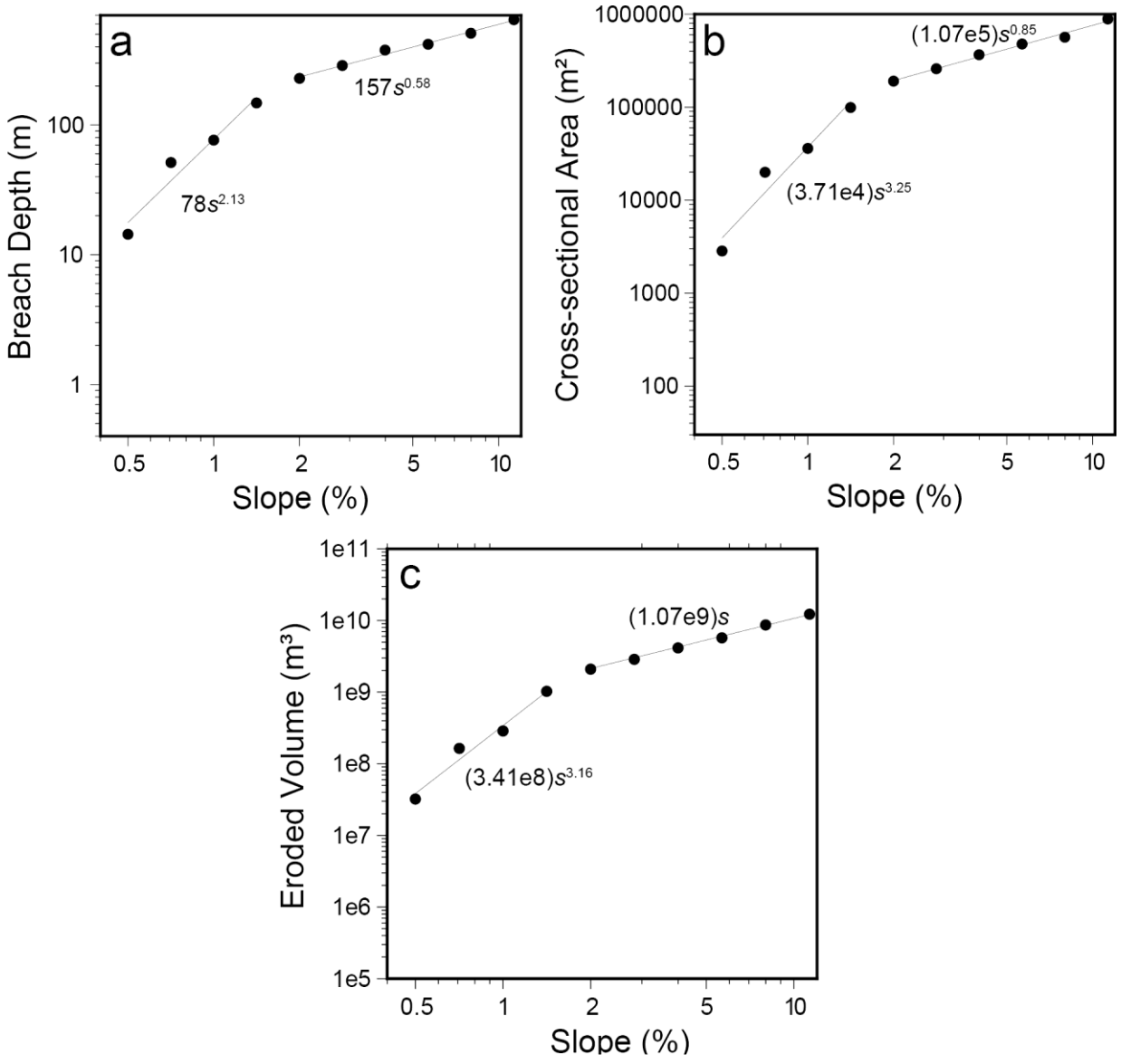

Figure 6. (a) Breach depth, (b) breach cross-sectional area, and (c) total eroded volumes as a function of exterior slope, for a 12 km radius lake and 8mm grain size. Steeper exterior slopes result in more erosion (as expected). The break in scaling at ~1.5% slope occurs where the lake is completely drained. Above that threshold, additional erosion is due to only the additional work in the exterior made possible by the steeper gradient. Below that threshold, the additional breach incision that is possible as slope steepens results in the release of more water, compounding the effect of slope.

having a very wide impoundment; on a low-sloped exterior, the lake floor is at a depth below more of the confining topography. Thus, at low slopes, even if the initial lake outflow is substantial, it is hard to maintain a runaway flood that catastrophically incises an outlet breach.

3.1.3 *Varying exterior confining slope (cross-slope)*

A second slope-related parameter that affects both the form and magnitude of the outlet valley's incision is the magnitude of the exterior confining slope or cross-slope, s_2 (see Fig. 3c; also apparent in the pre-breach topography in Fig. 4). Figure 7 shows how a cross-slope term, which helps focus initial flow and incision, has an effect on the resulting flood's behavior and final outlet morphometry. Broadly, a steeper (i.e., more confining) cross-slope results in more erosion. Qualitatively, this is easy to understand. Once the confining slopes are too shallow (< ~0.7% in these experiments; Fig. 7), the power of the overflow flood to move sediment is spread more broadly across the domain, and multiple channels become active (Fig. 8). Even during peak flood, the ability to cut down in any one channel is thus limited compared to narrowly confined cases. Because the amount of downstream erosion ultimately connects back to the breach, single channels can experience enhanced potential erosion at the breach compared to braided cases.

Interestingly, in each of these instances, the eroded volume:drained water ratio was essentially the same at 1.5% (this ratio is specific to the parameters used here, and equivalent to a sediment:water ratio of 1.2% because of the assumed porosity). But *where* sediment erodes is important to the removal of the impoundment: if erosion is not focused in a narrow channel that cuts across the impoundment, the deepening of the breach and runaway drainage of the lake is inhibited. For this reason, all idealized experiments except this one used a cross-slope of s_2 =1.5%.

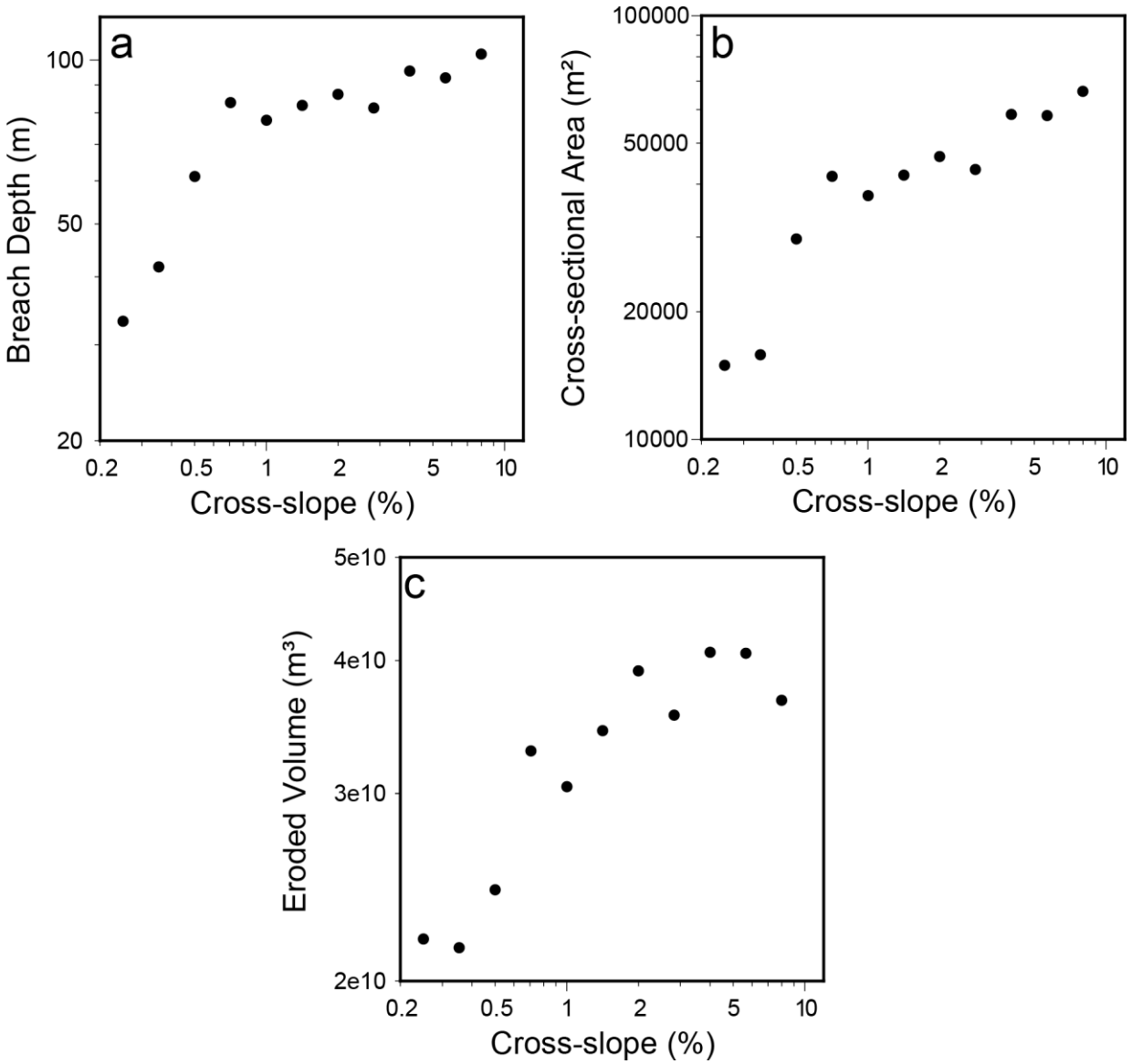

Figure 7. (a) Breach depth, (b) breach cross-sectional area, and (c) total eroded volumes as a function of exterior cross-slope, for a 12 km radius lake, 8mm grain size, and 1% exterior slope. Of particular note is that when the cross-slope magnitude is small (<0.7%), the flow spreads out and the incision on the exterior is limited by the poor channelization of the flow.

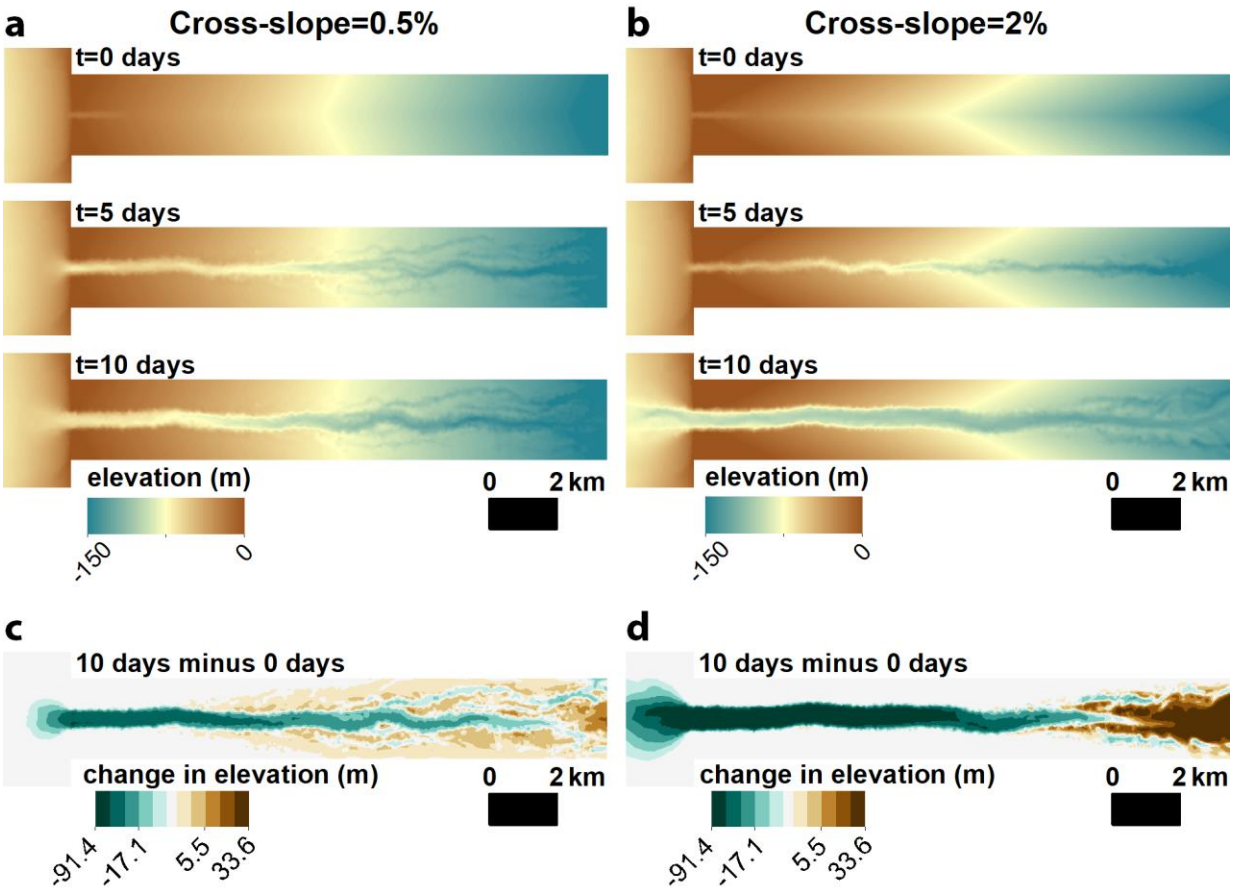

Figure 8. Experiment illustrating the differences in incision seen for the outlet part of the idealized domains for cross-slope experiments (R=12 km, 1% exterior slope). The width of each views is 18 km, starting 2km inside the lake. The amount of incision seen with small (0.5%)(a, c) and large (2%)(b, d) cross-slope terms differ substantially (see also Fig. 7). This arises for two reasons: (1) the initial channel that forms as the outlet grows in the low cross-slope experiment is wider and shallower, substantially reducing local shear stress across the channel, and (2) there is more channel switching, braiding and/or multiple active channels during the flood event with a lower cross-slope. This results in much less focused incision. Note the substantial incision on the inside of the basin for the higher cross-slope case after 10 days. Incision on the interior of lake basins is also common for the Mars numerical experiments, as well as in observations of Mars.

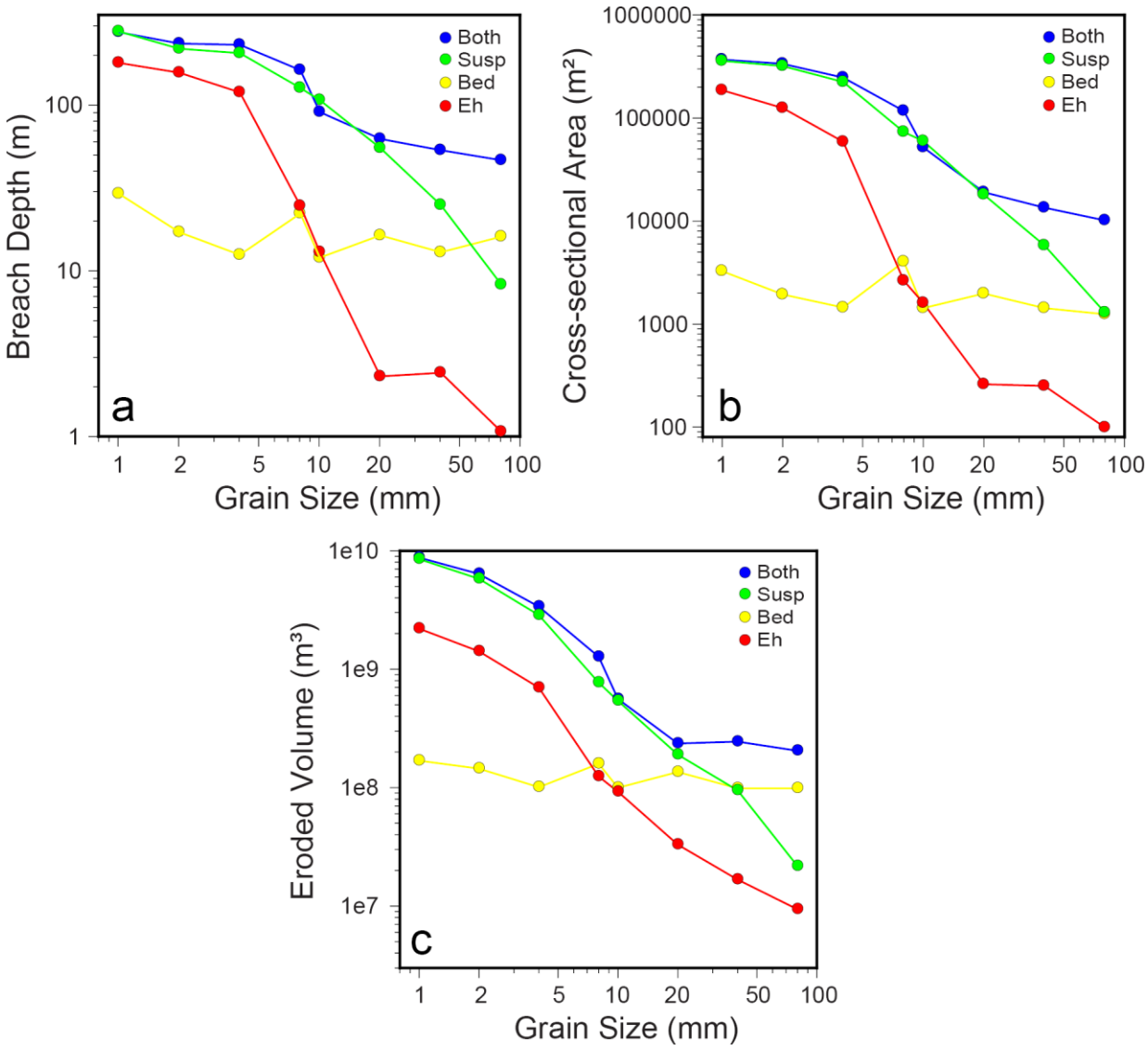

Figure 9. (a) Breach depth, (b) breach cross-sectional area, and (c) total eroded volume as a function of grain size. Note that incised breach depths >100m in (a) were cases where the lake drained fully for this particular idealized model (lake radius of 12 km).

3.2 Sediment transport

3.2.1. *Sediment Transport Mechanism and Grain Size*

Figure 9 shows how grain size and the formulation of the sediment transport mechanics translate into different resulting incision at a single lake size (radius 12 km) using otherwise default parameters. Four sediment transport formulations (see §2.2.1-2.2.2) that are plotted are: only bedload (Wong and Parker), only suspension, the Engelund-Hansen relation (calibrated

from experiments that included sediment moving in bedload and suspension), and using "both" the bedload & suspension operators (the default case in other experiments).

For the conditions modeled here, the bedload-only mechanism had a maximum of ~30m of breach incision, and the eroded volume was essentially independent of grain size *D*. This independence of bedload transport from specified grain size is not intuitive, but it arises from combining equations 2 to 5 with m=1.5, as follows: (1) In equation 2, the non-dimensional shear stress $\tau^* \propto D^{-1}$; (2) when well above the critical shear stress (see eq. 3), the nondimensional sediment flux q_b^* in equation 4 is $q_b^* \propto \tau^{*m}$, so $q_b^* \propto D^{-m}$, or plugging in m=1.5, $q_b^* \propto D^{-1.5}$. (3) For the dimensional sediment flux (equation 5), $q_b \propto q_b^* D^{1.5}$. So when most erosion is accomplished well above the critical shear stress, the grain size cancels out in the bedload-only regime (with a fixed Manning friction factor) (see also Wickert and Schildgen, 2019).

All of the other series in this set of sediment transport physics experiments were strongly dependent on grain size. Smaller grains are easier to transport as suspended sediment, as intuitively makes sense. The cases with suspension-only and both suspension & bedload behaved similarly for grain sizes smaller than 20mm: they generally had complete drainage. At those grain sizes, transport of sediment in the model was dominated by suspension. Above 20mm, more than an order of magnitude less erosion occurred than in the sand-dominated cases, presumably because net entrainment of suspended sediment only occurred in narrow parts of the domain near the breach, and for a shorter period of time. An interesting behavior for grain sizes ≥20mm was that the suspension-only model produced notably less erosion than when both suspension & bedload transport were enabled. At 40 and 80 mm grain sizes, when both transport operators were active, more erosion occurred than simple addition of the bedload-only and suspension-only cases would predict. A positive feedback between the two mechanisms led to higher sediment:water ratios and more water draining from the lake.

The Engelund-Hansen relation case had some qualitative similarities to the suspension-dominated cases for grain sizes below 8 mm, though the sediment:water ratios for the Engelund-Hansen case were a factor of ~3.8× lower, so eroded sediment volumes were lower by a similar factor. At grain sizes ≥8mm, there was a sharp decline in the ability to move sediment with this transport rule, presumably because there was insufficient shear stress to reach a positive feedback at the outlet breach. Outlet formation was almost entirely inhibited at the largest grain sizes. Presumably the grain size where this transition occurs is dependent on the specific setup of the domain as well as fixed parameters such as *K* in equation 4.

The roles of model physics and grain sizes shown here (Fig. 9) are worth exploring in this idealized context. However, whether a given lake overflow event experiences significant erosion and complete drainage or limited erosion and incomplete drainage depends not just on model physics and grain size. It also depends on numerous domain factors like lake size, lake hypsometry, the nature of the impoundment, and exterior slopes. This will become evident again when considering the Mars cases discussed in section 4.

3.2.2. *Gravity and Friction*

We ran a suite of tests to understand how the effect of using Mars gravitational acceleration compared to Earth's gravitational acceleration. Because the Manning coefficient is dimensional, changing the gravitational acceleration is intertwined with the handling of friction. We ran several comparisons of Earth and Mars with equivalent Manning coefficient values (n=0.0545 for Mars, and a gravity-corrected-equivalent of n=0.0335 for Earth; i.e., reduced by $(g_{Mars}/g_{Earth})^{0.5}$), and with the Wilson et al. friction model (supporting text S3).

When applying the Wilson et al. model, the Darcy-Weisbach coefficient *f* is calculated at every mesh element from the grain size and fluid depth *h* (supporting text S3). The Manning coefficient is then back-calculated with equation 9, which includes the correction for the difference in gravity between Earth and Mars. For constant depth, the reduction in the friction factor from Earth to Mars is the same as in the constant *n* case, though the absolute values are generally lower. The additional complication for the Wilson et al. case is that it has dependency on flow depth (and the evolving flow depth differs on Earth and Mars).

Results of these experiments are shown in Table 3. In all instances, more sediment is moved for the equivalent Mars lake compared to Earth; typically, the volume of additional sediment moved is increased by a factor of ~1.5-2×, although the results suggest this is lake size (event size) and physics-dependent.

Physics	Friction	LakeR	Grain Size	Eroded V: Water V Ratio_M	Eroded V: Water V Ratio_E	Breach Depth (d_M/d_E)	Eroded Volume (V_M/V_E)	Erosional Efficiency (Eroded V: Water V Ratio) (M/E)
bed	Constant	12 km	10 mm	0.022	0.016	**1.123**	**1.123**	**1.334**
both	Constant	12 km	10 mm	0.021	0.015	**1.128**	**1.492**	**1.421**
eh	Constant	12 km	10 mm	0.014	0.009	**6.343**	**2.498**	**1.547**
susp	Constant	12 km	10 mm	0.020	0.013	**1.494**	**1.780**	**1.573**
bed	Wilson	32 km	5 mm	0.024	0.015	0.685	**1.230**	**1.674**
eh	Wilson	32 km	5 mm	0.038	0.035	**3.530**	**1.474**	**1.094**
susp	Wilson	32 km	5 mm	0.115	0.063	**1.646**	**1.889**	**1.831**
bed	Wilson	64 km	5 mm	0.021	0.014	**2.658**	**2.968**	**1.542**
eh	Wilson	64 km	5 mm	0.029	0.026	**3.316**	**1.111**	**1.111**
susp	Wilson	64 km	5 mm	0.212	0.106	**1.883**	**2.055**	**2.001**

Table 3. Results for Mars (M) vs. Earth (E) gravity experiments for different model physics, lake sizes, and grain sizes. To the right of the thick solid line, all values are ratios of Mars compared to Earth for different model results. Bolded results are consistent with more sediment movement on Mars than Earth, which is seen in every test case. (bed: bedload operator; both: both bedload+suspension operators enabled ; eh: Engelund-Hansen operator; susp: suspension operator).

Lake Name (# in FH2008)	Lon (°E)	Lat (°N)	Lake Area (km^2)	Equivalent Radius (km)	References / Notes
Jezero (45)	77.7	18.4	1220	19.7	Fassett & Head (2005). Mars 2020 landing site. (Figs. 10, 14)
Unnamed, Libya Montes (25)	89.7	-0.1	955	17.4	Cabrol and Grin (2001). Fig. 1b; Suppl. Fig. 1.
Milna (65)	-12.3	-23.4	352	10.6	Buhler et al. (2014). Fig. 1c; Suppl. Fig. 4.
Unnamed, SW Thaumasia (61)	-103.0	-38.9	80	5.0	Connected to a system described by Mangold and Ansan (2006). Suppl. Fig. 2-3.
Unnamed, SW Thaumasia (N/A, "61A")	-103.3	-38.7	27	2.9	

Table 4. Open-basin lakes whose outlet formation was studied, from largest to smallest; see also Fig. 13; Supplementary Figures 1-4. Note that the smallest two lakes in the SW Thaumasia system (61, 61A) are probably Hesperian or younger (Mangold and Ansan, 2006), and may be due to glacial-lake overflow floods akin to the events studied by Warren et al. (2021) (both have concentric crater fill interpreted as ice rich on their floor today).

4. Results: Observed Mars Open Basin Lakes

We completed models for five example lakes (Table 4; Figs. 10-12) that allow us to examine the behavior of breach floods from open basin lakes on Mars on domains closer to natural topography (see, e.g., Supplementary Fig. 1-4; Supplementary movies 2-6; Fig. 13). We chose these lakes on the basis of having reasonable quality topography data and minimal complexity in their outlet regions that made setting up the model domain as feasible as possible. We also sought to have lakes of a range of sizes. We again stress that these are not meant to be exact reconstructions of these lakes' outlet-formative flood events, as the level of fidelity we expect is necessarily limited by model physics, uncertainty in the pre-flood domain, and resolution. However, there are advantages in examining close-to real topography, as it expands the range of behavior in the floods from what is observed on idealized terrain.

The pre-flood topography for lakes was estimated by using available topography data and infilling the breach and outlet canyon. We accomplished this by attempting to mask out the eroded outlet region and by artificially reconstructing the topography of these areas by inpainting the missing outlet regions based on the elevation of other nearby terrain. Other holes in the rim (e.g., young craters) were also filled as necessary. This pre-surface reconstruction is somewhat ad hoc, although the uncertainty in the pre-existing surface seems unlikely to have an outsized influence on the results, given all of the other inherent uncertainties. Earlier modeling efforts that utilize present-day Mars topography as a basis for modeling ancient landform evolution have used a similar approach (Barnhart et al., 2009). This pre-flood surface was converted to an ANUGA mesh, which was defined manually for each lake. Similar to our approach in the idealized model, we aimed for the mesh to have the higher resolution (smallest elements) in the area near the breach and outlet. Lower resolution areas were defined for the lakes themselves and the far field where water was allowed to pond for numerical reasons. The goal of studying these

events was to establish which sediment transport scenarios (varying only the physics, grain sizes, and/or initial breach stage) would form outlets with similar geometries to what is observed on Mars and determine reasonable hydrographs for these floods.

We established model scenarios that are most plausible given our assumptions by jointly comparing the outlet volumes and breach depths on Mars to those calculated in the model (Fig. 10-11). These 'best-fit' models (Table 5) were determined in a qualitative manner (from examination of Figs. 10 and 11). We think such a qualitative approach is reasonable, given that only grain size, model physics, and initial stage were varied, and even for those variables, a small part of the possible parameter space was explored. Additionally, the metrics for comparing Mars and the model are inherently coarse, so using a formal statistical method for determining the best-fit model is not really justified. We do note that the initial stage plays only a secondary role in the amount of incision if it was sufficient to lead to a runaway flood. This can be seen in Figures 10 and 11 – where there are two points for a given grain size and model physics, the slightly different outcomes come from 5-10m variations in the initial stage. Example flood hydrographs for each lake from these plausible scenarios are shown in Fig. 12. Movies for the best-fit cases for each lake are also included in the supplemental material.

Lake Name (# in FH2008)	Best-Fit Grain Size	
	Both	Eh
Jezero (45)	**80 mm**	20 mm
Unnamed, Libya Montes(25)	40 mm	**10 mm**
Milna (65)	**10 mm**	5 mm*
Unnamed, SW Thaumasia (61)	**20 mm**	10 mm
Unnamed, SW Thaumasia (N/A, "61A")	20 mm	**5 mm**

Table 5. Best-fit models for each of the lakes with Engelund-Hansen and both (suspension + bedload). See Fig. 10-12. (*Poor match). FH2008 = Fassett and Head (2008).

Overall, the model results (Figs. 10, 11) show that, in every instance, transport of sediment in suspension was necessary to achieve a model that fit the observed erosion plausibly well (recall the Engelund-Hansen relation was calibrated including suspension). Bedload-only cases were not erosive enough to match what is observed on Mars. Lake 65 (Milna) also failed to erode as much as expected with the Engelund-Hansen relation, perhaps because it did not reach a positive feedback between erosion and drainage. The Engelund-Hansen provided reconstructions consistent with observations in all four other cases.

The grain size where observations of Mars were most consonant with the model depended on model physics (Table 5). Model physics using the Engelund-Hansen relation generally matched better at smaller grain sizes than the best-fit model employing both suspension & bedload, consistent with expectations from idealized modeling (e.g., Fig. 9). The best-fit Engelund-Hansen models ranged from 5-20mm, whereas, for both suspension & bedload, the best fit models had 10-80mm grain size. Outlet characteristics were typically most in agreement with transport of grains in the gravel size range (with a few exceptions that extended the range up to small cobbles). We again caution that the applicability of these model grain sizes

to Mars may be inherently limited, given the uncertain sediment transport physics, single grain size used, and other erosional resistance terms that were not varied.

The peak fluxes for the best-fit models ranged from ~2×10^4 to ~5×10^6 m^3/s (Fig. 12) which is consistent with earlier estimates for the scale of these events (e.g., Irwin et al., 2004; Coleman, 2013, 2015). As expected, larger lakes had higher peak fluxes. The peak flux for the best-fit both suspension & bedload and Engelund-Hansen cases agree within a factor of 2–3×. In most instances, the overall form of the flux evolution is somewhat similar as well. The outlet-forming floods took days to a few weeks, with much of the erosion near the peak flux (Fig. 12; see also supplemental movies). This aligns well with Coleman (2013; 2015)'s estimates for Elaver Vallis and Tana Vallis.

Jezero crater's outlet-forming flood is useful to look at in detail as an example (Fig. 13). To set up the domain, Jezero's breach was filled in and its exterior was smoothed (Fig. 13a), and a mesh was defined with ~160m resolution in the outlet area and lower resolution triangles (~10 km) in the far-field. Inside the lake, a stage was defined starting just above the reconstructed topography, with enough initial hydraulic head to initiate sustained overflow. In reality, the initiation of the flood and the form of its early discharge are highly dependent on the mode of dam failure (e.g., over-topping vs. piping), which we do not capture here. As noted earlier, the initial hydraulic heads in our experiments play only a minor role in the observed outcome (Figs. 10, 11).

After the flood was initiated, the discharge in the outlet was above the threshold for sediment transport. Discharge grew as the outlet was incised in a positive feedback and took several Earth days to reach a peak of ~7×10^5 m^3/s and then declined slowly (Fig. 12). Incision in both the model and observations extends inside the confining topography, which is a powerful argument in favor of the outlet-forming catastrophically. The overall valley morphology, width, and depth compare reasonably well with observations. The main difference between the model and observations are that considerable channel switching is observed in the best-fit run (Fig. 13f) with suspension & bedload that is not obvious in observations (though not clearly precluded either). The best-fitting Engelund-Hansen model (Fig. 13g) has a straighter final outlet and may be a better morphological analogue to what is seen on Mars, even if it has a slightly worse fit to the total eroded volume.

The topography for the deposition seen at the eastern end of the modelled outlet in Fig. 13 is artificial, because it results from the reflective boundary condition on the domain causing a lake, in which sediment from the outlet is then deposited as an aggrading delta. In reality, the end of the observed Jezero outlet valley on the floor of Isidis is more indistinct, though evidence in CTX and HiRISE suggest the valley transitioned to deposition at its terminus as well. This transition may reflect a drop in the regional slope, building an alluvial deposit, rather than deposition in a standing body of water, although given the modified state of the outlet's terminus, deposition into standing water in the Mars case is hard to rule out with certainty.

Although multiple sediment transport equations reasonably match the eroded volume and breach depth of outlets (Figs. 10, 11), there were qualitative differences in the morphology of the outlet as a function of sediment transport mechanism (e.g., Fig. 13). For example, for Jezero and Lake 25, the suspension & bedload case produced erosion spread across multiple channels downstream of the breach, which resulted in less narrowly focused erosion than the best-fitting Engelund-Hansen model did for the same lake. On Mars, the outlets appear mostly characterized by single, deep canyons downstream of their breach, perhaps with some early-stage flow on surrounding surfaces (e.g., Irwin et al., 2004), so qualitatively, the Engelund-Hansen rule seems to match observed outlet morphology better than other transport laws, in at least some instances. Given the many simplifications involved here in treatment of erosion, particularly with respect to the use of a single grain size, the applicability of this observation is very uncertain.

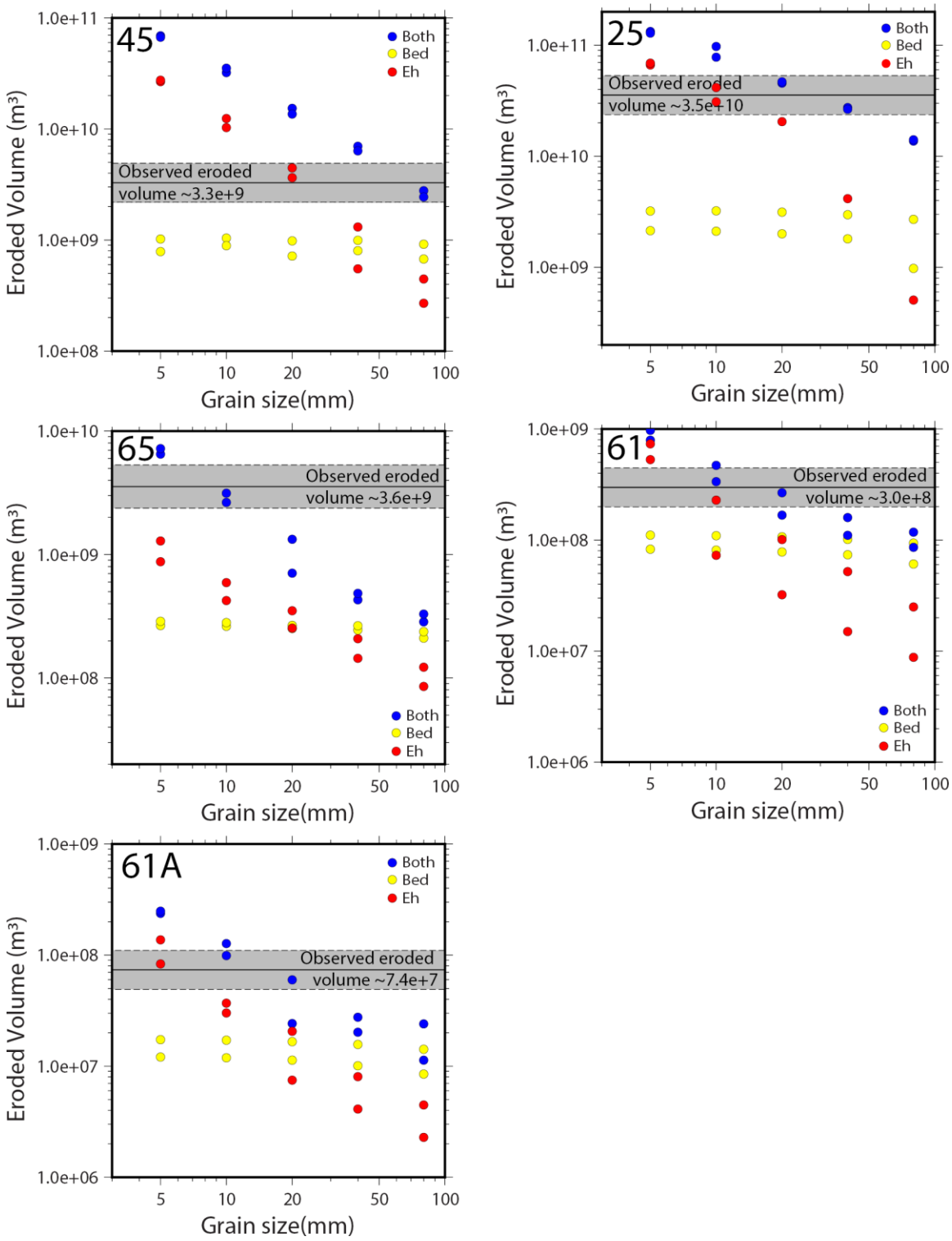

Fig. 10. The eroded volume results for domains where Mars open-basin lake topography was reconstructed. In each panel, lake number is in the upper left (Jezero is Lake 45). The two points for each grain-size represent different initial stages, which has only a modest effect compared to grain size and other domain properties. The solid line is the estimated eroded volume from topography data; the gray area is within a factor of 1.5× of this estimate. Bedload (yellow) by itself was never erosive enough to match observations.

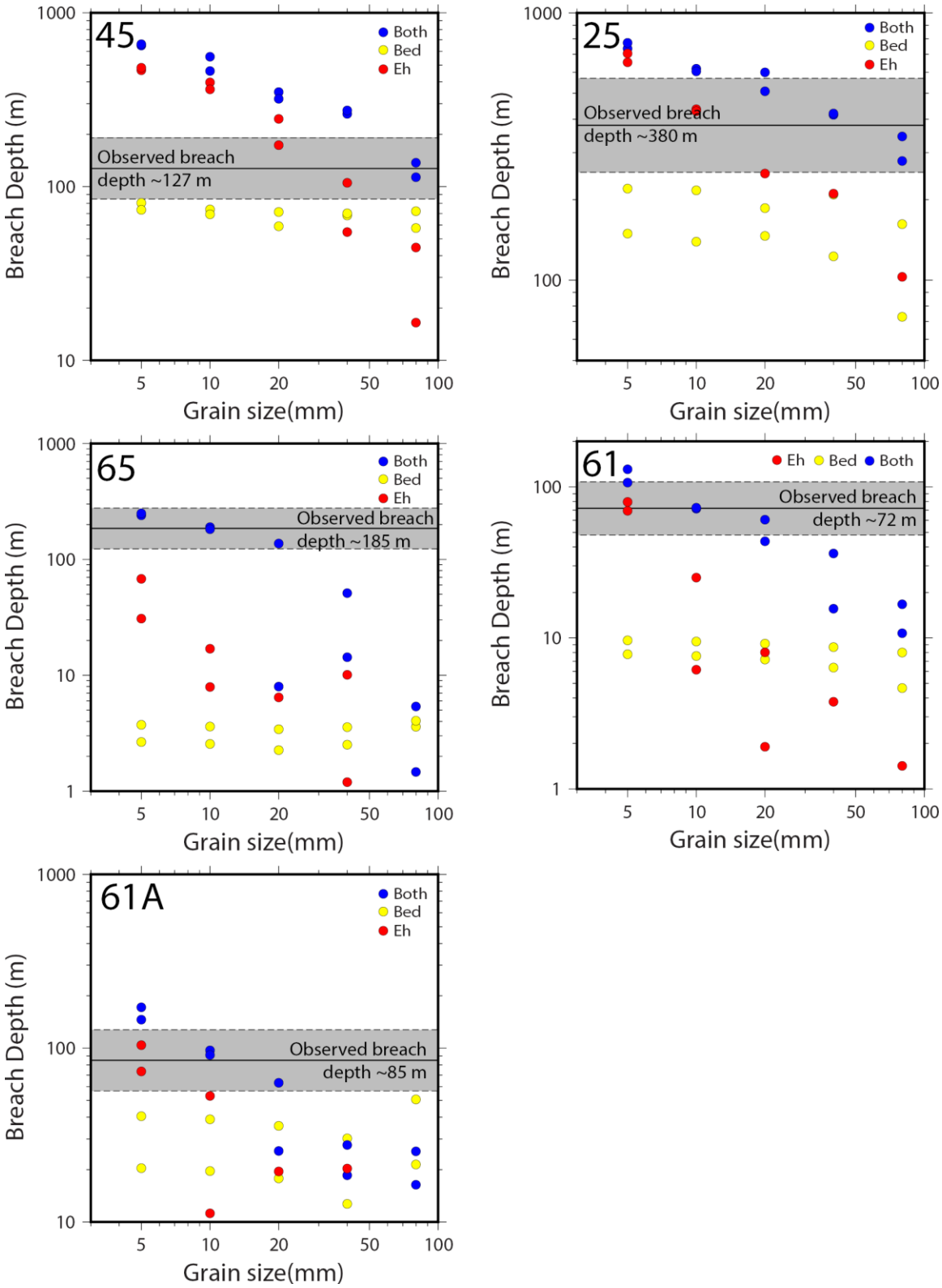

Fig. 11. Breach depth results for the reconstructed Mars open-basins lakes (lake number is in the upper left). The two points for each grain-size/physics are different initial stages. The solid line is the estimated breach depth from topography; the gray area is a factor of 1.5× around this estimate. Bedload did not erode the outlet deep enough to match observations.

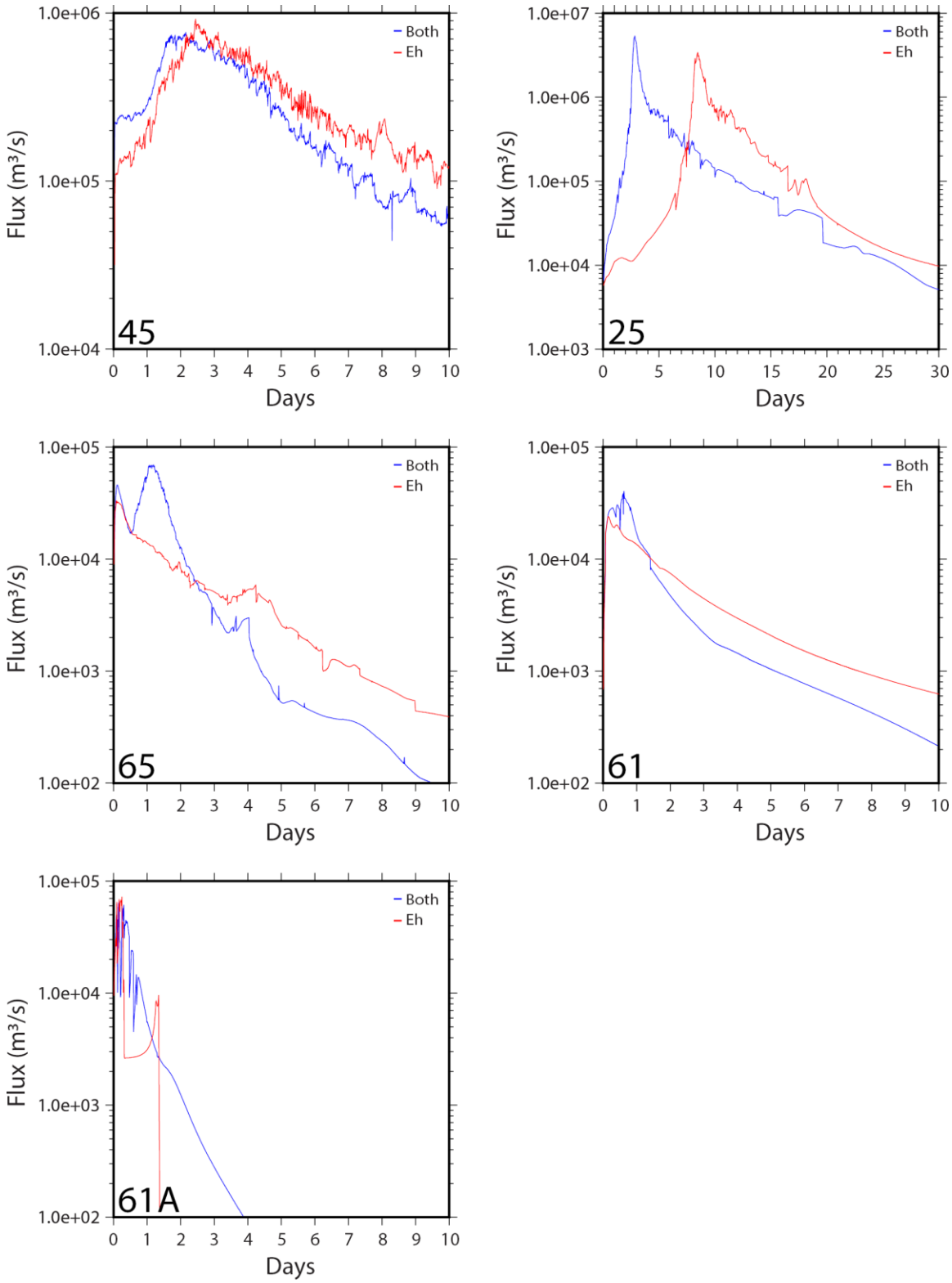

Fig. 12. Discharge (water flux) at the breach (lake number lower left), with the two series representing the best-fit Both (Suspension & Bedload) and Engelund-Hansen cases. The peak flux for these two scenarios agrees within a factor of 2-3×. In most instances, the overall form of the flux evolution is somewhat similar as well. The outlet-forming floods accomplished most of their erosion in periods of days to a few weeks.

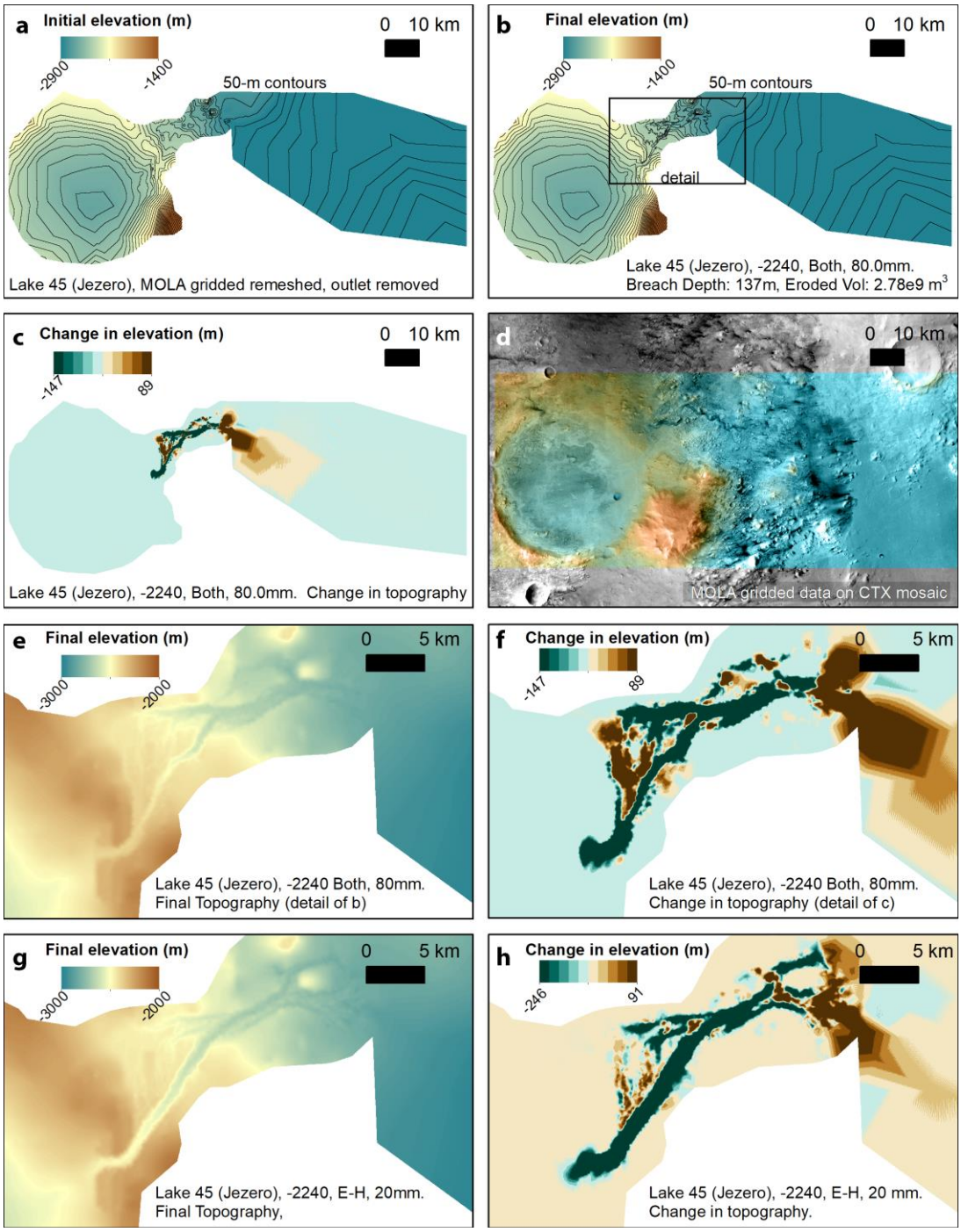

Figure 13. The best-fit ANUGA models for Jezero: 80-mm grains and Both suspension and bedload in (a)-(f); 20-mm grains and Engelund-Hansen as an alternative in (g) and (h). (a) Reconstructed topography before the breach-forming flood, removing the outlet. (b) Post-flood topography. (c) Difference between the post- and pre-flood surfaces. (d) Observed topography (MOLA gridded data; Smith et al., 2001) overlaid on a CTX mosaic (Dickson et al., 2018). Detailed view of the (e-f) Both/80-mm models and (g-h) Engelund-Hansen/20-mm models. The total erosion of the outlet, breach depth, and formative flux were similar with these two sediment transport modes, but the morphology of the outlet canyon differs. The Both case (e-f) had more prominent channel switching than the mostly single-threaded erosion experienced in the Engelund-Hansen case (g-h). Similar qualitative behavior was seen in other examples.

5. Discussion

5.1. Increasing Resistance to Erosion with Depth?

In both the idealized modeling and modeling of specific martian lakes, the eroded volume of outlets increased faster with lake size than simply expected from the additional available water in larger lakes. For example, Figure 5 shows the idealized model's morphometric results as a function of lake size and grain size. The increase in eroded volume (V_e) with initial, pre-breach lake volume (V_i) in these idealized model series has a power-law exponent ζ=1.26 to 1.66 (where $V_e \propto V_i^{\zeta}$), with the larger exponents occurring at larger grain sizes (hence the steepening in Fig. 5). In contrast, the Mars paleolake outlets measured by Goudge et al (2019) have a best-fit scaling of ζ=0.82 with considerable scatter. In other words, the amount of erosion in the Mars paleolake outlets increased sublinearly with lake size, and much less quickly than in the idealized model. In conjunction, there is a slight tendency in the observations of the larger lakes on Mars for a greater fraction of the initial water volume to remain in the lake following outlet incision. These observations are both contrary to the model results.

For the idealized lakes, one possible explanation is that the model's geometric scaling might not be adequately capturing what holds on Mars. For example, in the model, we assume that the length of the slope that outlets formed on scaled proportionally with lake size. This might not hold on Mars. Confining topography and slopes on the martian landscape may also not have been independent of lake size, unlike the assumptions in the model. However, this explanation does not explain that the same phenomena is observed in the modelled Mars cases.

A more interesting hypothesis that might explain this scaling discrepancy is if effective resistance to erosion (e.g., as parameterized by grain size in our model) increased with depth on Mars, unlike the constant value assumed in the model. In other words, if the outlet transitioned from eroding weaker regolith to more intact bedrock with depth (e.g., Clifford, 1993), erosion would become more difficult, limiting the possible erosion with increasing lake size, and improving the scaling agreement. There is a weak positive correlation between the size of the reconstructed Mars lakes and their best-fit grain size; in other words, larger lakes usually were reconstructed better with larger grain sizes in the domain, which might mimic the behavior of an increase in strength with depth for deeper outlets from larger lakes. There is presently no scheme in the model for handling depth-varying properties, but this might be a valuable area for future work.

The modeling generally predicts less efficient floods for the smallest lakes. Intriguingly, smaller open-basin lakes (areas <~100 km^2; radius of ~5.6 km) are less common on Mars. In the past, this observation has been attributed to bias resulting from resolution and preservation limits, rather than characteristic of early Mars (e.g., Cabrol and Grin, 2010). Although an observational or preservation bias is still the most likely explanation, an alternative is that small

lakes truly were less common as they had insufficient capacity to breach catastrophically and incise into their confining topography.

5.2. Pre-existing topography and surrounding slopes

Both exterior and cross-domain slope terms play an important role in the efficiency of outlet formation and whether a deep outlet can form. Indeed, the idealized results hint that an appreciable exterior slope (greater than a few tenths of a percent) may be a necessary pre-condition to erode enough of an outlet to get to a runaway flood and form a deep outlet. In other words, some craters that are currently classified as closed basins may have been able to accumulate enough water to overflow, but could not form a deep, narrow canyon because of their setting. Noachian craters whose rims had been substantially degraded may be susceptible to this, particularly if situated on plateaus or plains with very low surrounding slopes.

The cross-domain slope term also plays an important role in the form of the outlet valley that can incise, because an appreciable cross-slope helps confine erosion to a narrow portion of the outlet region. In early experiments, we realized that without any cross-domain slope, there was a strong tendency for water discharged from the lake's breach to spread broadly to the full width of the domain. The result was a wider outlet, shallower breach, and generally slower discharge to the outlet region (Fig. 8). The defocused flow has less capacity to carve a narrow canyon and hence deeply incise a breach, limiting the positive feedback between drainage and breach incision. This is clearly evident in Figure 7 and 8. Lakes with deep outlets only formed where non-negligible cross-slopes were available to focus flow. On natural landscapes, this might also be accomplished with sufficient topographic roughness or if pre-existing valleys and/or knickzones were able to focus flow during outlet evolution.

Qualitatively, the idealized experiments with low cross-slopes also look dissimilar to most preserved Mars' open-basin lake outlets, which usually have narrow outlet canyons, rather than broadly incised outlet plains. There are potential exceptions, such as the channel in Fig. 10 of Fassett et al. (2010), which is outside the 'hourglass'-shaped crater from Head et al. (2005). The bottom of the 'hourglass' has a rim-breaching outlet that fed braided channels on a wide outflow plain. This particular landform may be unusually young and the valley itself may be a glacial outburst flood, so it is atypical. For more typical ancient-Mars paleolakes, there is also likely an observational bias against recognizing overflowing lakes with broad, shallowly incised outlets.

Instead, high cross-slope terms, resulting in narrow and deep outlet canyons, are physically reasonable given the nature of the Mars cratered-highlands landscape. Many of the mapped open-basin lakes' breached and discharged onto surfaces previously incised by fluvial activity pre-dating the breach event. Pre-existing fluvial valleys provided one such natural source of confinement for outlets as they formed and evolved to focus flow. The importance of this type of rejuvenation of pre-existing valley paths has been emphasized before (e.g., Howard

et al., 2005; Irwin et al., 2005; Goudge and Fassett, 2018). Regardless, the results shown in Fig. 7 and Fig. 8 support the idea that capturing, incising, and enlarging these pre-existing valleys during outlet canyon formation would have enabled more efficient and deeper outlet incision than possible with floods discharging onto a pre-existing flat or regionally sloping planar surface. In this sense, the early stage of broad fluvial valley development may have primed the martian surface for highly erosive lake breach floods during the valley network era, and may be in part responsible for observations indicating the global importance of lake breach flood erosion (Goudge et al., 2021).

The idealized modeling lacked any natural topographic variability. Besides the scaling discussed in the previous section, one more way that the idealized modeling was unlike the Mars cases was that complete drainage of the lake and erosion of the impoundment was a common outcome. This is unlike the observed open-basin lakes on Mars, whose outlet must remain perched above the final lake floor to be recognized (a requirement in Fassett and Head, 2008). The best-fit Mars numerical models, in contrast to the idealized cases, do remain perched similar to the natural landscape. The details of the outlet region's topography may be as important to the end of floods as their initiation.

5.3. Sediment Transport on Mars vs. Earth

Comparisons of Mars and Earth sometimes suggest that the difference in gravitational acceleration largely cancels out of the sediment transport equations for equivalent forcing. At first glance, this looks justified by how changes in flow velocity and shear stresses interact. All else being equal, from the Darcy-Weisbach equation or from simple energy considerations, the mean velocity v is proportional to $g^{1/2}$. Thus flow would be expected to be slower on Mars for the same depth, slope, and friction. The nondimensional shear stress available to set sediment into motion is inversely proportional to g for a given velocity (eq. 2), because the force needed to loft and entrain a particle in the flow is lower under reduced gravity. Because the nondimensional shear stress $\propto v^2/g$ in equation 2, gravitational acceleration cancels out in terms of the effective shear on the bed.

However, that the gravitational differences between Mars and Earth cancel out in sediment transport seem unlikely to be correct upon closer scrutiny. The friction and flow characteristics are coupled, and the impact of both depend on gravitational acceleration, so a comparison that holds depth, slope, and friction constant is likely inappropriate. For example, Lapôtre et al. (2019) showed how expected channel geometry and threshold slopes on Mars are likely to be different than on Earth for a given constant discharge. The equilibrium slope for channels formed by suspension have also recently been shown to be different at reduced gravity (Amy and Dorrell, 2021). Komar (1980) and Amy and Dorrell (2021) both suggest a modestly higher efficiency of suspension-driven transport on Mars when considering the easier entrainment and settling under reduced gravity, even accounting for the slower expected flows.

Our results in section 3.2.2 support the idea that sediment transport is more efficient on Mars than Earth in large events both for bedload- and suspension-dominated scenarios. The median difference in eroded volume (V_M/V_E) we modelled (Table 3) was 1.64×. We note that this is close to $(g_M/g_E)^{0.5}$=1.63, but the difference in the particular test cases varied widely, so this result may be coincidental, and we lack a full theoretical explication of what should be expected given our model physics and our boundary conditions. Additional work on the theoretical amount of erosion expected on Mars versus Earth in complicated sediment transport scenarios such as these overflow floods would be a valuable future exercise. Ultimately fully testing these theories may require running some careful flume experiments in a laboratory with partial gravity, such as would be possible on Mars.

5.4. Importance of suspension

When exploring the model physics (§3.2.1) and looking at models of Mars open basin lake examples (§4), one obvious finding is that bedload-only cases are generally poor matches for what is seen on Mars because they are insufficiently erosive. Indeed, all the idealized modeling here is supportive of the interpretation that suspension was an important – perhaps predominant – sediment transport mechanism for martian outlet forming floods. Recall that models with either suspension enabled or with the Engelund-Hansen relation are the best matches to the reconstructed Mars lakes (e.g., Fig. 10-11).

To make a bedload-dominant scenario consistent with observations, it would require other changes in modelling or assumptions. The most drastic such possibility is that the outlet canyons formed gradually, requiring long lake lifetimes and lake recharge, rather than in catastrophic runaway events. This does not seem likely, because in a scenario with slow erosion, we would expect to see much weaker relationships between lake volume and outlet volume than is actually observed in Goudge et al., (2019), as recharge of the lake would become a more significant factor in how much erosion occurs than the lake's storage capacity. An additional, very clear indication that powerful floods formed outlets is multiple examples on Mars that have channelized erosion on their interior near their outlets, including Jezero. This is consistent with erosion due to focusing of flow at the basin outlet as water drained at high discharges. Erosion of the interior basin floor also is seen during physical experiments of lake overflow floods (Marra et al., 2014), and is unexpected in slow erosion scenarios. We also see this in the modeling here, ubiquitously (e.g., Figs. 4, 8, 13).

The importance of suspended sediment to erosion on Mars has been described before (Komar,1979, 1980; Burr et al., 2005; Amy and Dorrell, 2021). These past workers have shown that the threshold flow depths for suspension (and washload) are much lower on Mars than Earth because of its lower surface gravity, even accounting for the modestly higher particle densities expected for Mars sediments. Grain settling is also slower on Mars (Komar, 1980). This supports a common transition to suspension, washload, or debris-rich flows once a major dam-breach flood began on Mars.

6. Summary and Conclusions

In this paper, we have shown that outlets from open-basin lakes on Mars are consistent with having been carved by large lake breaching flood events, as previously suggested. To explore the dynamics of this process, we developed new operators that couple sediment transport to fluid flow in ANUGA. We used observations of idealized and reconstructed martian lakes to better understand the hydrodynamics and sediment transport of these floods in a transport-limited regime where transportable sediment was always available with sufficient shear stress.

A few key observations are as follows:

1. At least if decimeter and smaller sediment was available for transport, suspension was likely important for the formation of these outlets. Experiments where sediment transport was limited to bedload alone were not capable of carving the observed scale of outlets. Our results also suggest that sediment transport is more efficient on Mars than Earth in these type of events.
2. The detailed topography of the exterior of breached open-basin lakes was important to how much they incised. Regional slopes are important for the outlet's stream power, and the confinement of the outlet was necessary to focus flow and thus enable incision.
3. The grain size transported in our modeling that best-matched observations of Mars lakes were typically gravel-sized. Finer particles (sand) tended to drain crater lakes completely, and coarser particles (cobbles) tended to be unable to reach runaway erosion. However, the certainty of this result and its application to Mars is assumption-bound, given the limits of our parameterization of grain size in the modeling. Several of our results suggest erosional resistance may increase with depth in the martian crust.

Acknowledgments

We especially thank the developers of ANUGA and all other developers of open source software for making this work possible. We acknowledge R.P. Irwin and M. G. Kleinhans for helpful discussions related to this topic. We also thank Lisanne Braat and Isaac Larsen for perceptive and constructive formal review comments. Remaining misconceptions here are our own. This study was supported by NASA MDAP grant 80NSSC17K0442.

Data Availability

ANUGA is available at https://github.com/GeoscienceAustralia/anuga_core. The code developed for this study and example model inputs are available at https://github.com/cfassett/ANUGA-erosion; a permanent release is available at doi:10.5281/zenodo.5555066. No new observational data was derived during this study. Figures and other results can be replicated by re-running the model with appropriate inputs.

References

Amy, L., and Dorell, R. (2021), Equilibrium sediment transport, grade and discharge for suspended-load-dominated flows on Earth, Mars and Titan, *Icarus*, *360*, 114243, doi: 10.1016/j.icarus.2020.114243.

Barnhart, C. J., Howard, A. D., and Moore, J. M. (2009), Long-term precipitation and late-stage valley network formation: Landform simulations of Parana Basin, Mars, J. Geophys. Res., 114, E01003, doi:10.1029/2008JE003122.

Buhler, P., Fassett, C.I., Head, J.W., Lamb, M.P. (2014), Timescales of fluvial activity and intermittency in Milna Crater, Mars, *Icarus*, 241, 130–147, doi:10.1016/j.icarus.2014.06.028.

Burr, D.M., Emery, J.P., Lorenz, R.D., Collins, G.C., & Carling, P.A. (2006), Sediment transport by liquid surficial flow: Application to Titan, *Icarus*, *181*, 235-242.

Cabrol, N.A., & Grin, E. A. (1999), Distribution, classification, and ages of martian impact crater lakes, *Icarus*, *142*(1), 160–172.

Cabrol, N.A. & Grin, E.A. (2010), Searching for lakes on Mars: four decades of exploration, In: Lakes on Mars, N.A. Cabrol & E.A. Grin (eds.), 1–29. Oxford:Elsevier,

Clifford, S. M. (1993), A Model for the Hydrologic and Climatic Behavior of Water on Mars, *J. Geophys. Res.*, *98*, 10,973–11,016.

Coleman, N. M. (2013), Hydrographs of a Martian flood from a breached crater lake, with insights about flow calculations, channel erosion rates, and chasma growth, *J. Geophys. Res. Planets*, *118*, 263–277, doi:10.1029/2012JE004193.

Coleman, N.M. (2015), Hydrographs of a Martian flood from the breach of Galilaei crater, *Geomorphology*, *236*, 90–108, doi: 10.1016/j.geomorph.2015.01.034.

Dickson, J. L., Kerber, L. A., Fassett, C. I., & Ehlmann, B. L. (2018). A global, blended CTX mosaic of Mars with vectorized seam mapping: A new mosaicking pipeline using principles of non-destructive image editing, 49th Lunar and Planetary Science Conference, abs. no. 2048.

Dietrich, W.E. (1982), Settling velocity of natural particles, *Water Resources Research, 18*, 1615–1626, doi:10.1029/WR018i006p01615.

Engelund, F. & Hansen, F. (1967), A monograph on sediment transport in alluvial streams. Copenhagen, Denmark: Teknisk Forlag. 62 pp.

Fassett, C. I., and Head, J. W. (2005), Fluvial sedimentary deposits on Mars: Ancient deltas in a crater lake in the Nili Fossae region, Geophys. Res. Lett., 32, L14201, doi:10.1029/2005GL023456.

Fassett, C. I., & Head, J. W. (2008), Valley network-fed, open-basin lakes on Mars: Distribution and implications for Noachian surface and subsurface hydrology. *Icarus, 198*(1), 37–56. https://doi.org/10.1016/j.icarus.2008.06.016.

Fassett, C.I., Dickson, J.L., Head, J.W., Levy, J.S., Marchant, D.R. (2010), Supraglacial and proglacial valleys on Amazonian Mars, *Icarus*, 208, 86–100, doi:10.1016/j.icarus.2010.02.021

Fergason, R. L, Hare, T. M., & Laura, J. (2018). HRSC and MOLA Blended Digital Elevation Model at 200m v2. Astrogeology PDS Annex, U.S. Geological Survey. http://bit.ly/HRSC_MOLA_Blend_v0

Garcia-Castellanos, D. & O'Conner, J.E. (2018), Outburst floods provide erodability estimates consistent with long-term landscape evolution. *Sci. Reports, 8*, 10573, doi:10.1038/s41598-018-28981-y.

Goudge, T. A., Aureli, K. L., Head, J. W., Fassett, C. I., & Mustard, J. F. (2015), Classification and analysis of candidate impact crater-hosted closed-basin lakes on Mars, *Icarus*, *260*, 346–367. https://doi.org/10.1016/j.icarus.2015.07.026.

Goudge, T. A., & Fassett, C. I. (2018), Incision of Licus Vallis, Mars, from multiple lake overflow floods. Journal of Geophysical Research: Planets, 123, 405– 420. https://doi.org/10.1002/2017JE005438.

Goudge, T. A., Fassett, C. I., & Mohrig, D. (2019), Incision of paleolake outlet canyons on Mars from overflow flooding, *Geology*, *47*(1), 7–10. https://doi.org/10.1130/g45397.1.

Goudge, T. A., Morgan, A. M., Stucky de Quay, G., and Fassett, C.I. (2021), The importance of lake breach floods for valley incision on early Mars, *Nature, 597*, 645-649, doi:10.1038/s41586-021-03860-1.

Grotzinger, J. P., Gupta, S., Malin, M. C., Rubin, D. M., Schieber, J., Siebach, K., Sumner, D. Y., Stack, K. M. et al. (2015), Deposition, exhumation, and paleoclimate of an ancient lake deposit, Gale crater, Mars. *Science*, *350*, aac7575. https://doi.org/10.1126/science.aac7575.

Hanna, J. C., and R. J. Phillips (2005), Hydrological modeling of the Martian crust with application to the pressurization of aquifers, J. Geophys. Res., 110, E01004, doi:10.1029/2004JE002330.

Head, J.W. et al. (2005), Tropical to mid-latitude snow and ice accumulation, flow and glaciation on Mars, *Nature, 434*, 346-351.

Hilgendorf, Z., Wells, G., Larson, P.H., Millet, J., and Kohout, M. (2020), From basins to rivers: Understanding the revitalization and significance of top-down drainage integration mechanisms in drainage basin evolution, *Geomorphology, 352*, doi:10.1016/j.geomorph.2019.107020.

Holo, S., Kite, E.S. (2017), Incision of the Jezero Crater Outflow Channel by Fluvial Sediment Transport, *4th Early Mars*, abs. no. 3007,

Howard, A.D. (2007), Simulating the development of Martian highland landscapes through the interaction of impact cratering, fluvial erosion, and variable hydrologic forcing, *Icarus, 91*, 332–363, doi:10.1016/j.geomorph.2007.04.017.

Howard, A. D., Moore, J. M., and Irwin III, R. P. (2005), An intense terminal epoch of widespread fluvial activity on early Mars: 1. Valley network incision and associated deposits, *J. Geophys. Res., 110*, E12S14, doi:10.1029/2005JE002459.

Irwin, R.P., Maxwell, T.A., Howard, A.D., Craddock, R.A., and Leverington, D.W. (2002), A Large Paleolake Basin at the Head of Ma'adim Vallis, Mars, *Science*, *296*, 2209–2212, doi:10.1126/science.1071143.

Irwin, R.P., Howard, A. D., and Maxwell, T. A. (2004). Geomorphology of Ma'adim Vallis, Mars, and associated paleolake basins, *J. Geophys. Res., 109*, E12009, doi:10.1029/2004JE002287.

Irwin, R.P., Howard, A. D., Craddock, R. A., and Moore, J. M. (2005), An intense terminal epoch of widespread fluvial activity on early Mars: 2. Increased runoff and paleolake development, *J. Geophys. Res., 110*, E12S15, doi:10.1029/2005JE002460.

Irwin, R.P., Grant, J.A. (2009), Large basin overflow floods on Mars, in: *Megaflooding on Earth and Mars*, Baker,V.R., Carling, P., Burr, D. (eds). Cambridge: Cambridge Univ. Press, 209–224.

Irwin, R.P., Craddock, R.A., Howard, A.D., Flemming, H.L. (2011), Topographic influences on development of Martian valley networks, *JGR-Planets, 116*, E02005, doi:10.1029/2010JE003620.

Johnson, B.C., Milliken, R.E., Lewis, K.W., and Collins, G.S. (2021), Impact generated porosity in Gale crater and implications for the density of sedimentary rocks in lower Aeolis Mons, *Icarus, 366*, 114539, doi:10.1016/j.icarus.2021.114539.

Johnson, J. P. L. (2014), A surface roughness model for predicting alluvial cover and bed load transport rate in bedrock channels, *J. Geophys. Res. Earth Surf.*, 119, 2147– 2173, doi:10.1002/2013JF003000.

Kleinhans, M. G. (2005), Flow discharge and sediment transport models for estimating a minimum timescale of hydrological activity and channel and delta formation on Mars. *J. Geophys. Res, 110,* E12003, doi:10.1029/2005JE002521.

Komar, P.D. (1979), Comparisons of the hydraulic of water flow in martian outflow channels with flows of similar scale on Earth. *Icarus, 37,* 156–181.

Komar, P.D. (1980), Modes of sediment transport in channelized water flows with ramifications to the erosion of the martian outflow channels. *Icarus*, *42*, 317–329.

Lamb, M.P., and Fonstad, M.A. (2010), Rapid formation of a modern bedrock canyon by a single flood event. *Nature Geoscience*, *3*, 477–481, doi: 10.1038/ngeo894.

Lapôtre, M. G. A., and Lamb, M. P. (2015), Hydraulics of floods upstream of horseshoe canyons and waterfalls, *J. Geophys. Res. Earth Surf.*, 120, 1227–1250, doi:10.1002/2014JF003412

Lapôtre, M. G. A., Lamb, M. P., and Williams, R. M. E. (2016), Canyon formation constraints on the discharge of catastrophic outburst floods of Earth and Mars, *J. Geophys. Res. Planets, 121*, 1232– 1263, doi:10.1002/2016JE005061.

Lapôtre, M. G. A., Ielpi, A., Lamb, M. P., Williams, R. M. E., & Knoll, A. H. (2019), Model for the formation of single-thread rivers in barren landscapes and implications for pre-Silurian and Martian fluvial deposits. Journal of Geophysical Research: Earth Surface, 124, 2757–2777. https://doi.org/10.1029/2019JF005156.

Larsen, I.J. and Lamb, M.P. (2016), Progressive incision of the Channeled Scablands by outburst floods, *Nature*, *538*, 229–232, doi:10.1038/nature19817.

Lewis, K. W., Peters, S., Gonter, K., Morrison, S., Schmerr, N., Vasavada, A. R., & Gabriel, T. (2019), A surface gravity traverse on Mars indicates low bedrock density at Gale crater. *Science*, *363*, 535–537. https://doi.org/10.1126/science.aat0738

Mangold, N., Ansan, V. (2006), Detailed study of an hydrological system of valleys, a delta and lakes in the Southwest Thaumasia region, Mars, *Icarus*, 180, 75–87.

Marra, W.A., Braat, L., Baar, AW., Kleinhans, M.G. (2014), Valley formation by groundwater seepage, pressurized groundwater outbursts and crater-lake overflow in flume experiments with implications for Mars. *Icarus, 232,* 97–117, doi:10.1016/j.icarus.2013.12.026.

Meyer-Peter, E., Mueller, R.(1948), Formulas for bed-load transport, in Proceedings 2nd Meeting, pp. 39–64, Int. Assoc. for Hydraul. Struct. Res., Stockholm.

O'Connor, J.E. & Beebee, R.A. (2009), Floods from natural rock-material dams, in: *Megaflooding on Earth and Mars*, Baker,V.R., Carling, P., Burr, D. (eds). Cambridge: Cambridge Univ. Press, 128–171.

Parker, G. (1998), Lecture Notes on the Interaction of Flow and Sediment Transport in Rivers and the Ocean, Summer Short Course on Environmental Fluid Dynamics, International Centre for Mechanical Sciences, Udine, Italy, 1998. http://hydrolab.illinois.edu/people/parkerg/course_notes.htm (last retrieved: 4/27/2020).

Parker, G. (2005), 1D Sediment Transport Morphodynamics, With Applications to Fluvial and Subaqueous Fans and Fan-Deltas (e-book), http://hydrlab.illinois.edu/people/parkerg/morphodynamics_e-book.htm (last retrieved: 4/27/2020).

Perignon, M. (2016), Using the sediment transport and vegetation operators in ANUGA, https://github.com/mperignon/anugaSed/blob/master/docs/anugaSed_manual.pdf (last retrieved: 4/27/2020).

Rigby, E. & Van Drie, R. (2008), ANUGA: A New Free and Open Source Hydrodynamic Model, in: Proceedings of Water Down Under 2008, Lambert, M., Daniell, T. M., Leonard, M. (eds). Modbury, SA: Engineers Australia ; Causal Productions, 2008, 629-638.

Rigby, E., Mazengarb, C., Barthelmess, A., and Kain, C (2017), Experiences developing and applying an Anuga Dune Erosion Operator to assess risk from loss of dune protection during a tsunami. 13th Hydraulics in Water Engineering Conference, Sydney, Australia, 99–106.

Roberts, S., Nielsen, O., Gray, D., Sexton, J., Davies, G. (2019), ANUGA User Manual (v. 2.0.3; March 26, 2019), https://github.com/GeoscienceAustralia/anuga_core/blob/master/doc/anuga_user_manual.pdf.

Rogers, A. D., Warner, N. H., Golombek, M. P., Head, J. W., & Cowart, J. C. (2018). Areally extensive surface bedrock exposures on Mars: Many are clastic rocks, not lavas. Geophysical Research Letters, 45, 1767– 1777. https://doi.org/10.1002/2018GL077030

Shewchuk, J. R. (1996), Triangle: Engineering a 2D quality mesh generator and Delaunay triangulator, In Workshop on Applied Computational Geometry (pp. 203–222). Berlin, Heidelberg: Springer.

Seekell, D. A., & Pace, M. L. (2011), Does the Pareto distribution adequately describe the size-distribution of lakes? *Limnology and Oceanography*, *56*(1), 350–356. https://doi.org/10.4319/lo.2011.56.1.0350.

Smith, J. D., & McLean, S. R. (1977), Boundary Layer Adjustments to Bottom Topography and Suspended Sediment. Elsevier Oceanography Series, 123–151. doi:10.1016/s0422-9894(08)70839-0.

Smith, D.E., et al. (2001), Mars Orbiter Laser Altimeter—Experiment summary after the first year of global mapping of Mars, *Journal of Geophysical Research*, *106*(E10), 23689–23722, doi: 10.1029/2000JE001364.

Stucky de Quay, G., Goudge, T.A., & Fassett, C.I. (2020), Precipitation and aridity constraints from paleolakes on early Mars, *Geology*, *48*, 1189–1193, doi: 10.1130/G47886.1.

Van Der Walt, S., S. C. Colbert, and G. Varoquaux (2011). The NumPy array: A structure for efficient numerical computation, *Comput. Sci. Eng.*, 13, 22– 30.

Van Drie, R., Milevski, P., Simon, M. (2013), A single Open Source Tool with diverse range of application: ANUGA; Detailed Hydraulics to Catchment Wide Hydrology, 2013 Novatech Conference, Lyon, France.

Warren, A.O., Holo, S., Kite, E.A., Wilson, S.A. (2021), Overspilling small craters on a dry Mars: Insights from breach erosion modeling. *Earth and Planetary Science Letters, 554*, 116671, doi:10.1016/j.epsl.2020.116671.

Whipple, K.X., Hancock, G.S., & Anderson, R.S. (2000), River incision into bedrock: Mechanics and relative efficacy of plucking, abrasion, and cavitation. GSA Bulletin, 112, 490-503.

Wickert, A.D. & Schildgen, T.F., 2019. Long-profile evolution of transport-limited gravel-bed rivers. *Earth Surface Dynamics, 7*, 17–43, doi:10.5194/esurf-7-17-2019.

Wong, M. & G. Parker (2006), Reanalysis and Correction of Bed-Load Relation of Meyer-Peter and Müller Using Their Own Database, J. Hydraulic Eng., 132, https://doi.org/10.1061/(ASCE)0733-9429(2006)132:11(1159).

JGR-Planets

Supporting Information for

Modeling the Hydrodynamics, Sediment Transport, and Valley Incision of Outlet-forming Floods from Martian Crater Lakes

Caleb I. Fassett[1]
Timothy A. Goudge[2,3,4]

[1]NASA Marshall Space Flight Center, Huntsville, AL 35805
[2]Department of Geological Sciences, Jackson School of Geosciences, The University of Texas at Austin, Austin, TX, USA
[3]Center for Planetary Systems Habitability, The University of Texas at Austin, Austin, TX, USA
[4]CIFAR Azrieli Global Scholars Program, CIFAR, Toronto, Ontario, Canada

Contents of this file

Introduction
Text S1 to S5
Supplementary Table 1, 2
Supplementary Figs. 1-4
Supplementary Movies 1-6

Introduction

The supplementary sections include equations from the literature that are used for (a) settling of sediment (S1) and (b) friction factors (S2). The relationship defined for the suspended sediment distribution with Rouse number is provided in function form (S3). Additional parameter variation experiments with grain density (S4) and porosity (S5) are also included, along with associated data tables (density; Supp. Table 1; porosity; Supp. Table 2).

Additionally, Supplementary Figures 1-4 show images and domain characteristics for each of the modelled Mars lakes (a similar figure of this type for an idealized lake (Fig. 4) and Lake 45/Jezero are included as Fig. 10 in the main manuscript). The supplementary movies show animations of the domain evolution, both for an idealized example and best-fit models for each of the Mars domains. In the movies, the mesh elevation is shown as a color ramp (blue = low elevation, yellow = high elevation) and the fluid momentum is shown as arrows (black, scaled for visibility).

Text S1. Settling Velocity for Suspended Sediment

Calculation of the settling velocity v_s follows Dietrich (1982). The first two equations describe the nondimensional effective grain size, D_*, and nondimensional settling velocity V_*.

V_* is given by Dietrich (1982)'s equation 5. Note that ρ_s and ρ are density of the sediment and fluid, respectively, g is the acceleration of gravity, and ν is the kinematic viscosity:

$$V_* = \frac{\rho\, {v_s}^3}{(\rho_s - \rho) g \nu} \qquad \text{eq. S1}$$

D_* is given by his equation 6, for grain size D:

$$D_* = \frac{(\rho_s - \rho) g D^3}{\rho\, \nu^2} \qquad \text{eq. S2}$$

We apply Dietrich (1982)'s equation 8 (pure Stokes' settling) for the smallest grains ($D_* \leq 0.05$):

$$V_* = \frac{{D_*}^2}{5832} \qquad \text{eq. S3}$$

For larger grains ($D_* > 0.05$), we use Dietrich (1982)'s equation 9:

$$\log V_* = -3.76715 + 1.92944 \log D_* - 0.09815 (\log D_*)^2 - 0.00575 (\log D_*)^3 + 0.00056 (\log D_*)^4 \qquad \text{eq. S4}$$

The maximum grain size where Dietrich (1982)'s analysis applies is $D_* = 5 \times 10^9$, which corresponds to a grain size of D=8.1cm on Mars for spherical grains of $\rho_s = 3000$ kg/m^3. This is the upper limit where the suspended sediment model here is applicable and sets the upper limit on the size range for grains explored.

Text S2. *d as a function of Rouse number (Z)**

The sediment concentration profile parameter, *d** (see Ganti et al., 2014) was defined as a function of Rouse number Z, where $\boldsymbol{Z = v_s/\kappa u_s}$. v_s is the settling velocity from Dietrich described above (text S1), κ=0.41 (von Karman's constant), and $\boldsymbol{u_s = \sqrt{\tau/\rho}}$. *d** is a multiplier on the average concentration, so that the bottom layer concentration is increased by a factor of *d** above the average (i.e., in the limit of complete mixing, *d**=1, and when *d** is large, almost all sediment near the bed is in the bottom layer and exchangeable with the bed). The function used is as follows (see also Fig. 2 of the main text):

Z<0.8:	$d^*=3.057(Z^2)+3.4803Z+1$
Z>=0.8 & Z<2.0:	$d^*=-1.4802(Z^2)+11.181Z-2.3601$
Z>=2.0 & Z<4.0:	$d^*=-0.9557(Z^2)+8.0402Z+1.8783$
Z>=4.0 & Z<6.0:	$d^*=-0.1753(Z^2)+2.1908Z+12.908$
Z>6:	$d^*=19.76$

Text S3. Friction Factors

The calculation of the Darcy-Weisbach friction factor (as $\sqrt{\frac{8}{f}}$) follows from Wilson et al., (2004) and is a function of grain size.

For the largest grain size (boulders, D > 6.4cm), we use Wilson et al. (2004)'s equation 15:

$$\sqrt{\frac{8}{f}} = 5.62 \log_{10}\left(\frac{R}{D}\right) + 4.0 \qquad \text{eq. S5}$$

For gravel (2 mm ≤ D ≤ 6.4 cm), we use Wilson et al. (2004)'s equation 14:

$$\sqrt{\frac{8}{f}} = 5.75 \log_{10}\left(\frac{R}{D}\right) + 4.514 \qquad \text{eq. S6}$$

For sand (D ≤ 2 mm), we use Wilson et al. (2004)'s equation 13:

$$\sqrt{\frac{8}{f}} = 8.46 \log_{10}\left(\frac{R}{D}\right)^{0.1005} \qquad \text{eq. S6}$$

Text S4. Effect of Grain Density

The relative density of sediment grains and water affects the efficiency of transport directly through the shear stress (eq. 2 of the main text). Intuitively, grain density matters because of the force balance between the (negative) buoyancy of grains, and the lifting forces induced by the fluid. We ran one numerical experimental series changing ρ_s. As expected, the difference in the total eroded volume was (approximately) inversely proportional to $(\rho_s - \rho)$ (see Supplementary Table 1 below). The expected grain densities on Mars are ~3000 kg/m^3; a change in particle density of $\Delta\rho_s$ ~ 100 kg/m^3 introduced a median of ~3% difference in the ultimate amount of eroded volume. Given this limited sensitivity to particle density, we chose to use a constant ρ_s=3000 kg/m^3 in all other model runs. As already discussed, we also fixed the density of the fluid to ρ=1000 kg/m^3 in all model runs. Handling the physics involved in highly concentrated flows or debris flows is beyond the scope of what we attempt here.

Text S5. Effect of Porosity

Porosity of the near-surface alters the ease of erosion through the Exner equation (eq. 6 of the main text). Increased porosity reduces the mass of sediment required to be transported for a given volume of erosion. The actual porosity of Mars likely varies with depth (e.g., Clifford, 1993; Hanna and Phillip, 2005) as well as on different geologic units. There are few measurements of porosity on Mars, so it is a highly uncertain parameter. The porosity of the near-surface crust at Gale crater has been estimated from rover accelerometer measurements. Depending on assumptions, porosity of ~18± 6% to 40± 6% have been inferred (Lewis et al., 2019; Johnson et al., 2021). It is not clear how representative this is of the Noachian highlands as a whole. For this reason, we arbitrarily choose a porosity of 20% for all model runs, with the exception of a few experiments run here. We also impose the requirement that the porosity of eroded and deposited materials is the same; however, this is not expected to significantly impact our results assessing net erosion.

As a sensitivity test, we ran 25 experiments across a range of lake sizes and grain sizes with porosity doubled from 20% to 40% (Supplementary Table 2 below). There was only slight change in the breach depth at higher porosity (5% enhancement); the reason breach depth did not increase much is likely because it was limited by the geometry of the lake. Breach width increased on average by 10%, and the total volume of erosion in the outlet increased by a median of 26%, traceable to greater sediment transport for a given discharge through the outlet as expected. As with density, the observed changes of <30% in erosional efficiency are well within the uncertainty caused by other poorly constrained parameters relevant to these events, which justifies keeping a fixed value across the rest of the model runs here.

LakeR	Grain Size	Sediment Density	Breach Depth	Sed. Vol	Water Vol	Eroded V: Water V
12 km	1 mm	2700	275.356	8.96E+09	2.73E+10	0.329
	1 mm	2800	277.499	9.04E+09	2.73E+10	0.331
	1 mm	2900	278.227	8.82E+09	2.73E+10	0.323
	1 mm	3000	285.490	8.85E+09	2.73E+10	0.324
	1 mm	3100	274.582	8.59E+09	2.73E+10	0.314
	1 mm	3200	273.176	8.08E+09	2.74E+10	0.295
	1 mm	3300	273.738	8.64E+09	2.74E+10	0.316
	2 mm	2700	251.241	6.58E+09	2.77E+10	0.238
	2 mm	2800	249.167	6.38E+09	2.77E+10	0.231
	2 mm	2900	255.551	6.21E+09	2.76E+10	0.225
	2 mm	3000	258.316	6.12E+09	2.76E+10	0.222
	2 mm	3100	250.423	5.76E+09	2.76E+10	0.208
	2 mm	3200	250.983	5.71E+09	2.76E+10	0.207
	2 mm	3300	251.914	5.51E+09	2.76E+10	0.200
	4 mm	2700	229.761	3.51E+09	2.77E+10	0.127
	4 mm	2800	206.454	3.10E+09	2.76E+10	0.112
	4 mm	2900	205.905	3.08E+09	2.76E+10	0.112
	4 mm	3000	195.362	2.96E+09	2.75E+10	0.108
	4 mm	3100	207.692	2.80E+09	2.74E+10	0.102
	4 mm	3200	193.134	2.46E+09	2.73E+10	0.090
	4 mm	3300	191.400	2.44E+09	2.73E+10	0.089
	8 mm	2700	134.148	9.19E+08	2.42E+10	0.038
	8 mm	2800	135.949	8.73E+08	2.42E+10	0.036
	8 mm	2900	103.901	7.30E+08	2.14E+10	0.034
	8 mm	3100	95.995	7.12E+08	2.30E+10	0.031
	8 mm	3200	98.573	6.59E+08	2.27E+10	0.029
	8 mm	3300	101.470	6.27E+08	2.31E+10	0.027
	10 mm	2700	89.964	6.82E+08	2.27E+10	0.030
	10 mm	2800	98.933	6.11E+08	2.26E+10	0.027
	10 mm	2900	103.242	5.29E+08	2.16E+10	0.025
	10 mm	3000	104.797	5.69E+08	2.17E+10	0.026
	10 mm	3100	123.805	7.68E+08	2.40E+10	0.032
	10 mm	3200	80.762	4.85E+08	2.17E+10	0.022

Supplementary Table 1. Numerical experiments changing grain density. Changes of $\Delta\rho_s$=100 kg/m^3 introduce a median of ~3% difference in the eroded volume. The eroded volume:water volume ratio is similar to a sediment:water ratio (by volume); specifically, the sediment:water ratio is is 0.8× the EV:WV ratio accounting for the default porosity.

LakeR	Grain Size	Eroded V: Water V Ratio, 40% porosity	Eroded V: Water V Ratio, 20% porosity	Breach Depth (d_40%/d_20%)	Eroded Volume (V_40%/V_20%)	Erosional Efficiency (Eroded V: Water V Ratio) (40%/20%)
1 km	1 mm	0.110	0.084	**1.081**	**1.279**	**1.297**
1 km	2 mm	0.035	0.021	**1.143**	**1.658**	**1.665**
2 km	1 mm	0.164	0.138	**1.034**	**1.158**	**1.193**
2 km	2 mm	0.078	0.056	**1.114**	**1.378**	**1.392**
2 km	4 mm	0.022	0.014	**1.191**	**1.622**	**1.627**
3 km	1 mm	0.200	0.166	**1.015**	**1.155**	**1.206**
3 km	2 mm	0.102	0.080	**1.093**	**1.257**	**1.274**
3 km	4 mm	0.039	0.022	**1.184**	**1.751**	**1.763**
4 km	1 mm	0.233	0.193	**1.028**	**1.131**	**1.208**
4 km	2 mm	0.131	0.098	**1.063**	**1.312**	**1.336**
4 km	4 mm	0.050	0.029	**1.151**	**1.669**	**1.684**
6 km	2 mm	0.164	0.127	**1.009**	**1.266**	**1.297**
6 km	4 mm	0.075	0.054	**1.058**	**1.383**	**1.396**
8 km	1 mm	0.299	0.249	**1.054**	**1.097**	**1.198**
8 km	2 mm	0.180	0.152	**1.077**	**1.161**	**1.185**
8 km	4 mm	0.096	0.072	**1.136**	**1.349**	**1.335**
12 km	1 mm	0.339	0.287	**1.013**	**1.101**	**1.183**
12 km	2 mm	0.235	0.202	**1.006**	**1.153**	**1.160**
16 km	1 mm	0.361	0.308	0.950	**1.127**	**1.174**
16 km	2 mm	0.290	0.231	**1.045**	**1.245**	**1.257**
16 km	4 mm	0.162	0.126	0.982	**1.278**	**1.285**
20 km	1 mm	0.377	0.331	0.947	**1.109**	**1.139**
20 km	2 mm	0.320	0.263	0.976	**1.204**	**1.216**
20 km	4 mm	0.185	0.152	0.962	**1.217**	**1.217**
20 km	8 mm	0.091	0.069	**1.122**	**1.337**	**1.316**

Supplementary Table 2. Results comparing different assumed porosities (bolded results are consistent with more erosion/sediment movement in higher porosity cases). All 25 experiments saw higher outlet volumes eroded with higher porosity, as expected, with a median increase of ~26% (1.26×); breach depth was not typically changed by much, because the lake overflow eroded through the entire confining topography.

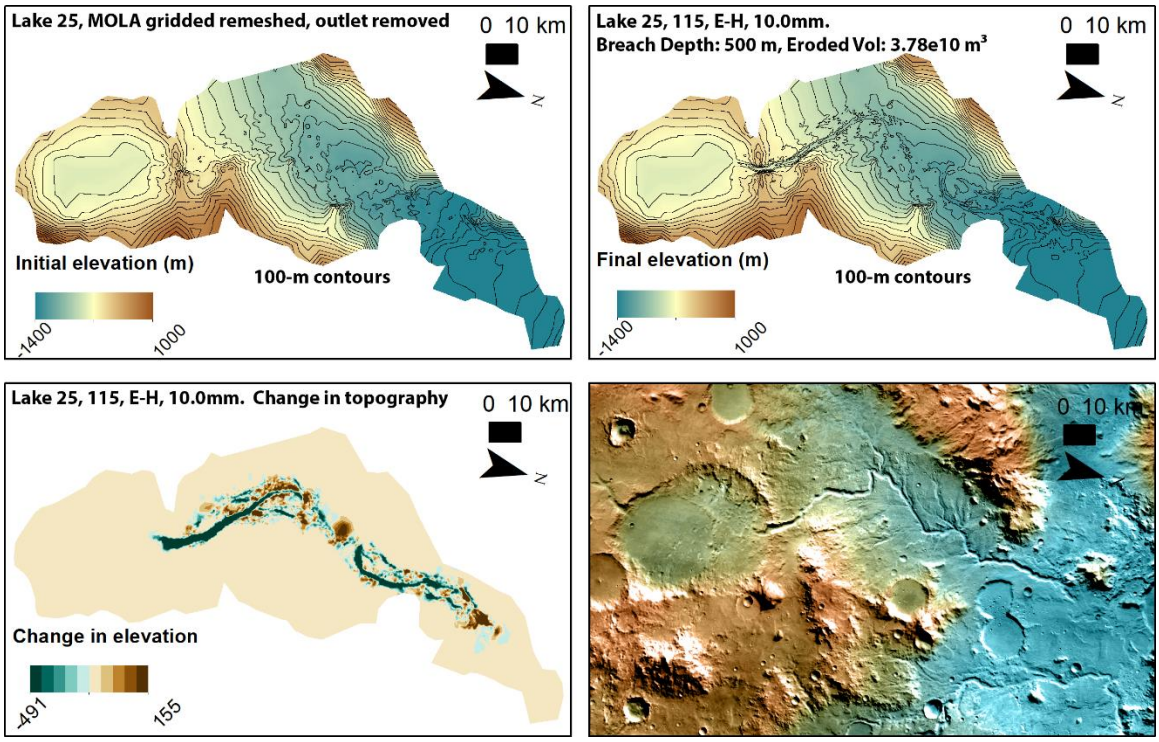

Supplementary Figure 1. Lake 25. (upper left) Initial reconstructed domain. (upper right) Best-fit model. (lower left) MOLA overlaid on CTX mosaic.

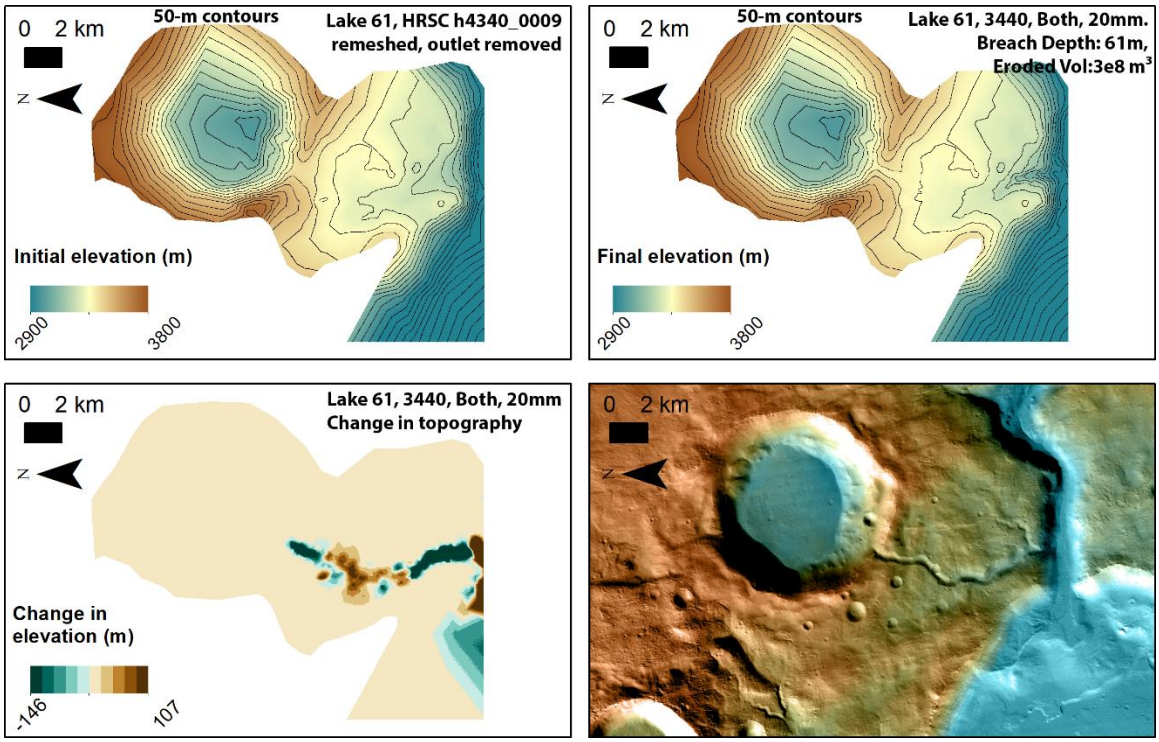

Supplementary Figure 2. Lake 61. (upper left) Initial reconstructed domain. (upper right) Best-fit model. (lower left) HRSC h4340_0009 overlaid on CTX mosaic.

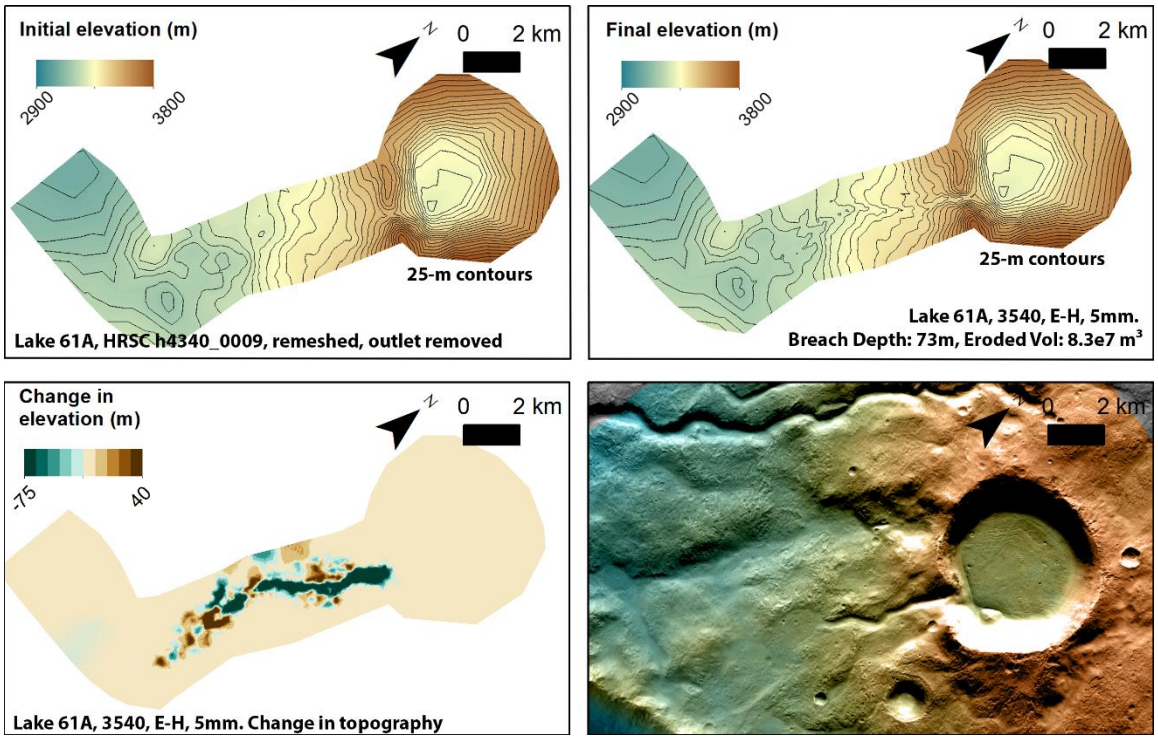

Supplementary Figure 3. Lake 61A. (upper left) Initial reconstructed domain. (upper right) Best-fit model. (lower left) HRSC h4340_0009 overlaid on CTX mosaic.

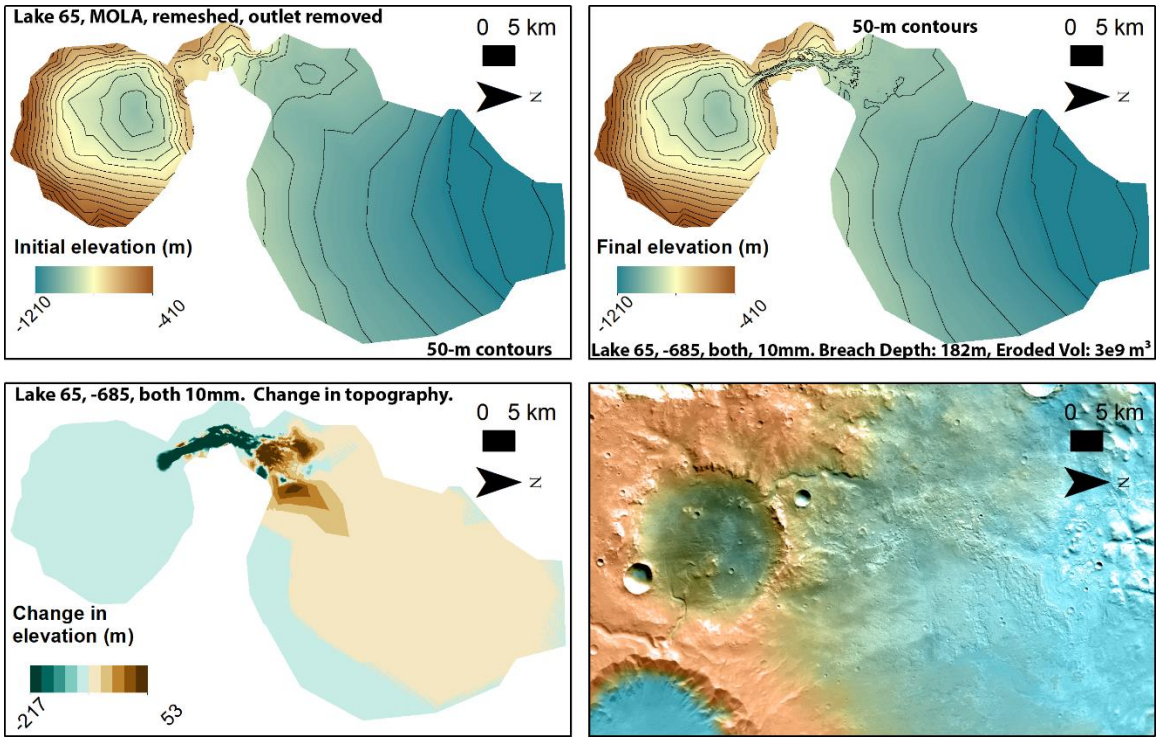

Supplementary Figure 4. Lake 65 (Milna). (upper left) Initial reconstructed domain. (upper right) Best-fit model. (lower left) MOLA overlaid on CTX mosaic.